Effect of alpha-tubulin acetylation on the doublet microtubule structure

Shun Kai Yang[1,Ψ], Shintaroh Kubo[1, Ψ], Corbin Black[1], Katya Peri[1], Daniel Dai[1], Melissa Valente[1], Jacek Gaertig[3], Khanh Huy Bui[1,2*]

Author affiliations
1. Department of Anatomy and Cell Biology, McGill University, Montréal, Québec H3A 0C7, Canada
2. Centre de Recherche en Biologie Structurale, McGill University, Montréal, Québec H3A 0C7, Canada
3. Department of Cellular Biology, University of Georgia, Athens, GA, USA

[Ψ] These authors contributed equally

*Corresponding author:
Khanh Huy Bui, Department of Anatomy and Cell Biology, McGill University, Montréal, Québec H3A 0C7, Canada. E-mail: huy.bui@mcgill.ca

Key words: Cilia, Doublet microtubule, Acetylation, Post-translational Modification, Cryo-electron Microscopy

Abstract

Acetylation of α-tubulin at the lysine 40 residue (αK40) by ATAT1/MEC-17 acetyltransferase modulates microtubule properties and occurs in most eukaryotic cells. Acetylated microtubules are more stable and damage resistant. αK40 acetylation is the only known microtubule luminal post-translational modification site. The luminal location suggests that the modification tunes the lateral interaction of protofilaments inside the microtubule. In this study, we examined the effect of tubulin acetylation on the doublet microtubule in the cilia of *Tetrahymena thermophila* using a combination of cryo-electron microscopy, molecular dynamics, and mass spectrometry. We found that αK40 acetylation exerts a small-scale effect on the doublet microtubule structure and stability by influencing the lateral rotational angle. In addition, comparative mass spectrometry revealed a link between αK40 acetylation and phosphorylation in cilia.

INTRODUCTION

Cilia have diverse roles in cell motility, sensory functions, signalling, and growth control. Motile cilia drive the flow of fluid, including human sperm (Lehti & Sironen, 2017), mucus clearance in the respiratory tract (Bustamante-Marin & Ostrowski, 2017), and cerebrospinal fluid circulation (Djenoune & Wyart, 2017). Non-motile primary cilia in rod cells are critical for transmitting chemical signals converted from light (Sjostrand, 1953). In kidney epithelial cells, cilia function as mechanosensors for transmitting fluid flow signals into signalling pathways. At the core, motile and primary cilia share the same cytoskeletal framework, the axoneme (Porter & Sale, 2000), composed of a bundle of nine outer doublet microtubules (DMTs). Each DMT is composed of protofilaments (PFs) of tubulins that form into a hollow cylinder A-tubule and an incomplete cylinder B-tubule (Fig. 1A). Inside the DMT lumen, a weaving network of microtubule inner proteins (MIPs) stabilizes the DMT structure (Ichikawa et al., 2019; Ichikawa et al., 2017; Ma et al., 2019).

Tubulins undergo several highly conserved post-translational modifications (PTMs) that collectively represent the so-called ‘tubulin code”, in which PTMs modulate microtubule properties directly or indirectly through the binding of microtubule-associated proteins (MAPs). The common and well-studied tubulin PTMs are phosphorylation, detyrosination, glutamylation, glycylation and acetylation (Wloga, Joachimiak, Louka, & Gaertig, 2017). DMT contains a unique signature of PTMs including cilia-specific PTMs such as glycylation. For example, the B-tubule of DMT is enriched with glutamylated

(Lechtreck & Geimer, 2000) and detyrosinated (Johnson, 1998) tubulins, while A-tubule tubulins are mostly unmodified. PTM is a fine tune for ciliary function rather than a biphasic switch. Glutamylation could regulate inner dynein arm activities, which control the ciliary waveform (Tomohiro Kubo, Yanagisawa, Yagi, Hirono, & Kamiya, 2010; Lechtreck & Geimer, 2000; Suryavanshi et al., 2010). Hyperglutamylation due to depletion of deglutamylases can improve intraflagellar transport in ift88-deficient zebrafish (Pathak, Austin-Tse, Liu, Vasilyev, & Drummond, 2014). Lack of glycylation causes abnormal pre-powerstroke and post-powerstroke conformations of dynein arms in mouse sperm (Gadadhar et al., 2021). The loss of glycylation sometimes leads to an increase in glutamylation, possibly because the two PTMs compete for the same set of modification sites (glutamic acids) on tubulins (T. Kubo, Hirono, Aikawa, Kamiya, & Witman, 2015; Rogowski et al., 2019; Rogowski et al., 2010a; Wloga, Webster, et al., 2009). These observations suggest that there is an interplay between PTMs and cilia properties.

One of the most intriguing PTMs in cilia is acetylation, which occurs inside the lumen of DMT on the lysine 40 residue of α-tubulins (αK40). αK40 acetylation in *Chlamydomonas reinhardtii* cilia was the first identified tubulin acetylation (M & Piperno, 1987; Sw & Rosenbaum, 1983). Tubulin acetylation was later found on different microtubules in cells, such as in neurons (Fukushige, Hendzel, Bazett-Jones, & McGhee, 1999). Acetylation could also take place on lysine 60 and lysine 370 residues of α-tubulin and lysine 58 of β-tubulin (Liu et al., 2015). Acetylation is interesting because the αK40 loop is the only luminal PTM site and is close to the tubulin lateral interaction interface (Kaul, Soppina, & Verhey, 2014) (Fig. 1B). The αK40 loop is flexible and close to the tubulin

lateral interaction interface (Eshun-Wilson et al., 2019; Howes, Alushin, Shida, Nachury, & Nogales, 2014) and is almost 100% completely acetylated in cilia (Akella et al., 2010). Acetylated αK40 has been shown to enhance microtubule stability and longevity *in vitro* (Schaedel et al., 2015), while deacetylated microtubules decrease in rigidity and are prone to complete breakage events (Xu et al., 2017).

The main enzyme responsible for αK40 acetylation is alpha-acetyltransferase-1 (αTAT1), also known as MEC-17 (Akella et al., 2010). Deacetylation is carried out by histone deacetylase 6 (HDAC6) (Hubbert et al., 2002) and nicotinamide adenine dinucleotide-dependent deacetylase sirtuin 2 (SIRT2) (North, Bl, Mt, Jm, & Verdin, 2003). Mice that lack αTAT1 have defective sperm flagellar beating (Kalebic et al., 2013), and *C. elegans* become touch insensitive without αTAT1 (Akella et al., 2010; Shida, Cueva, Xu, Goodman, & Nachury, 2010). Motor proteins travel preferentially on acetyl-K40 microtubules because of their higher binding affinity (Garnham & Roll-Mecak, 2012; Reed et al., 2006). Overexpression of HDAC6 or SIRT2 could lead to short cilia (Ran, Yang, Li, Liu, & Zhou, 2015; Zhou et al., 2014), but the cilia-shortening effect of HDAC6 could be countered by an acetyl-K mimic α-tubulin, suggesting that it may destabilize the microtubule lattice (Cueva, Hsin, Huang, & Goodman, 2012).

The αK40 loop is functionally important, but it is flexible and disordered even in both acetylated and deacetylated reconstituted microtubules (Eshun-Wilson et al., 2019; Howes et al., 2014). Cryo-EM and molecular dynamic studies of acetylated microtubules suggest that acetylation restricts the αK40 loop motion by disturbing the electrostatic interaction (Eshun-Wilson et al., 2019). This produces more ordered loops and stabilizes the microtubule lattice. In certain organisms, such as *C. elegans*,

acetylation of αK40 would disrupt an intramonomer salt bridge from αE55 to αK40 (Cueva, Hsin, et al., 2012). Replacing αK40 with arginine or in the absence of acetyl-αK40 could result in the formation of a salt bridge from αE55 with αK40, αR40, or αH283, to change the interprotofilament angle leading to elliptical microtubules and variation in the number of PFs (Cueva, Hsin, et al., 2012).

Interestingly, many αK40 loops are fully structured in the cryo-EM map of the DMT from ciliate and green algae (Khalifa et al., 2020; Ma et al., 2019). This result suggests that the αK40 loop may have an important role in recognizing and binding with different MIPs to stabilize cilia, and disruption of acetylation may disrupt the interaction between the αK40 loop and MIPs.

In this work, we aimed to clarify the role of αK40 acetylation in the assembly and stability of ciliary DMT. To answer our questions, we studied the structural effect of acetylated and non-acetylated tubulins on DMT and MIPs from wild-type *Tetrahymena thermophila*, mutants lacking tubulin acetyltransferase (MEC-17) and αK40-specific de-acetylation (*K40R*) (Akella et al., 2010) by a combination of cryo-EM, molecular dynamics and mass spectrometry.

RESULTS

Acetylated αK40 loops are structured when interacting with certain MIPs

We first examined a 48-nm repeat cryo-EM density map from native DMTs of *Tetrahymena* WT (*CU428* strain) (Fig. 1A) (S. Kubo et al., 2023). We identified and modeled all visible αK40 loops of α-tubulins in the map, which are known to be almost 100% acetylated (Akella et al., 2010; Gaertig et al., 1995). Most *Tetrahymena* MIPs have been localized and identified in this map (S. Kubo et al., 2023). In contrast to the acetylated singlet microtubule structure (Eshun-Wilson et al., 2019), we observed many fully structured αK40 full (missing no more than two residues from residues 37 to 48) and partial structure loops (missing 3-5 residues) in DMT (Fig. 1C-G). In certain PFs, including A1, A3, A5, A11, and B1, all αK40 loops are structured. Interestingly, the structured αK40 loops are much less abundant in the B-tubule (Fig. 1G). There is a pattern in the distribution of αK40 loops: likely due to their flexibility, ordered αK40 loops are visible at positions where MIPs and tubulins interact but are difficult to resolve in places with little or no MIPs. (Fig. 1H, Table S1). Notably, in A1, where RIB72A and RIB72B are in contact with αK40 (Fig. 1C, D), all αK40 loops are fully structured, in agreement with the 8-nm alternating pattern of Rib72A and Rib72B (Fig. 1G). This pattern is consistent with previous observations of the αK40 loops in the green algae *Chlamydomonas reinhardtii* DMT (Khalifa et al., 2020; Ma et al., 2019). Therefore, the B-tubule has fewer ordered αK40 loops compared to the A-tubule, probably due to fewer MIPs in the B-tubule.

A superimposition of the conformations of all fully structured αK40 loops in the DMT revealed that they adopt multiple conformations (Fig. 2A). The exact structures of αK40 loops might adapt to both the inter-PF angle and interactions with the contacting MIPs. We did not observe any conformations where acetylated αK40 was directly involved in tubulin-tubulin lateral interactions (Fig. 2A, Fig. 1C-F).

We noticed that the αK40 loop is always structured when interacting with DM10 domains of the MIPs, suggesting that DM10 is a αK40 loop interacting domain. Superimposing all seven DM10 domains (three from RIB72A, three from RIB72B and one from CFAP67) (Fig. 2B) showed that while there are some variations in other parts of DM10 domain, the region interacting with the αK40 loop are conserved in its topology (Fig. 2B, C). Sequence alignment of the DM10 domains suggests that an aromatic residue (phenylalanine or tyrosine) is conserved and might be responsible to the interaction with the DM10 domain (Fig. 2C, D, E).

To determine whether the conformation of the αK40 loops is conserved between species, we compared the αK40 loops in the DMTs of *Tetrahymena thermophila* and *Chlamydomonas reinhardtii* (Fig. 2F, G, H). The αK40 loop conformations from B9 and B10 are similar between the two species, and both interact with the conserved CFAP52. These results suggest that the αK40 loop conformation is tuned by its interactions with adjacent MIPs. The interaction between MIPs and the αK40 loop implies that acetylation might play a role in DMT assembly or stability or both.

K40 acetylation alters the inter-PF angles in the B-tubule

With our observation that acetylated αK40 in the DMT of wild type *Tetrahymena* cells adopts a fixed conformation when interacting with MIPs, we evaluated whether the absence of αK40 acetylation affects the MIPs and hence the overall DMT structure. We obtained the DMT structures from the *Tetrahymena MEC17-KO* and *K40R* mutants at 4.5 and 3.5 Å resolution, respectively. In *MEC17-KO*, an ortholog of the mammalian α-TAT1 α-tubulin K40 acetyltransferase, is knocked out to abolish detectable αK40 acetylation, while in the *K40R* mutant, lysine 40 on ATU1 (the single canonical α-tubulin isotype in *Tetrahymena*) is mutated to arginine to prevent acetylation at the αK40 position (Akella et al., 2010).

Our first observation is that all the MIPs look intact in both the *MEC17-KO* and *K40R* mutants (Fig. 3A). This observation is consistent with the phenotypes that the *MEC17-KO* and *K40R* cilia look similar to the WT cilia (Akella et al., 2010; Gaertig et al., 1995). Therefore, our cryo-EM analyses indicate that acetylation does not affect DMT and MIP assembly.

Next, we examined the tubulin structure by comparing the αK60 and αK40 loop structures at PFs A3 and B1 (Fig. 3B-I, Fig. S2). Previously, it was reported that αK40 acetylation led to a reduction in the distance of αK60 from the M-loop of the adjacent tubulin from 12 Å to 8 Å (Eshun-Wilson et al., 2019). Our comparison of (acetylated and non-acetylated) αK40 and αK60 loops did not reveal significant structural differences.

However, this result does not rule out a change in αK40 and αK60 conformation, which is likely too small to be observed accurately at this resolution.

Since αK40 loops are suggested to be involved in lateral interactions (Cueva, J., & Huang, 2012; Eshun-Wilson et al., 2019), acetylation might affect inter-PF angles. We measured the inter-PF angles in the DMTs of the *WT* and the two acetylation-deficient mutants. We observed only minor changes in the inter-PF angles in the A-tubule (Fig. 4A). However, in the B-tubule, the changes in the inter-PF angles were more prominent (Fig. 4A-J). Most notably, the change in the inter-PF angle between PFs B7 and B8 and B9 and B10 ranges from 3 to 6 degrees (Fig. 4H-J, Table S2). These are significant changes in specific PF curvatures.

We also inspected the tubulin lattice by measuring the distances between adjacent tubulin dimers. There were small changes in the inter-dimer distances in PFs A1, A3, A5, A8, B3 and B7 between WT and mutants (Fig. S3, Table S3). This scale of changes in the tubulin lattice is significantly smaller (0.3 – 0.5 Å) than the known impacts of the nucleotide state (Zhang, Alushin, Brown, & Nogales, 2015) and missing MIPs (Ichikawa et al., 2019) (~2 Å difference). This is similar to the observation of differences in interdimer distances in 96% acetylated and 99% de-acetylated microtubules using *in vitro* reconstitution.

Overall, our analysis shows that tubulin lattice changes, specifically inter-PF angles, can be used as an indication of microtubule stability when acetylation is lacking.

Acetylated αK40 loops are less flexible

While we observed some structural differences between acetylated and non-acetylated DMT, our resolution does not allow us to see small changes in the αK40 loops. Therefore, we attempted to detect structural differences using molecular dynamic simulations.

We performed an all-atom molecular dynamic simulation for α-tubulin with acetylated and non-acetylated αK40 to determine whether acetylation changes the loop behavior (Fig 5A, B). To determine how acetylation of αK40 affects the structure of the αK40-loop, we used the K-means clustering method for the αK40-loop region based on the Cα position. To avoid bias in clustering, the structures obtained during the simulated trajectories with acetylated and non-acetylated αK40 were mixed, and 10 clusters were created (Fig. 5A). Interestingly, clusters comprise mostly acetylated or non-acetylated conformations but not mixed populations. This indicates that acetylated and non-acetylated αK40 loops adopt distinctively different conformations. In addition, the most populated cluster consists of only ~ acetylated conformations and ~50% of all acetylation conformations, while the non-acetylated αK40 loops form five clusters of less than 30% conformations. Therefore, the acetylated αK40 loop adopts more rigid conformations than non-acetylated αK40 loop. It appears that this finding is similar to that of a previous study (Eshun-Wilson et al., 2019) despite differences in molecular dynamic setups of porcine and ciliate tubulins and clustering methods.

Acetylation of αK40 does not affect tubulin and MIPs

Since we did not observe any structural changes in the MIPs of *MEC17-KO* and *K40R* mutants, non-acetylated αK40 does not seem to significantly weaken the binding of MIPs. Therefore, we further explored the degree to which the interaction between the αK40 loop and MIP is affected by acetylation using coarse-grain molecular dynamic simulation to compare the energy between tubulins and CFAP52 with the acetylated αK40 and the non-acetylated αK40 structures (Fig. 5C).

We found that both acetylated and non-acetylated αK40 have a stabilizing effect when binding to CFAP52. On the other hand, when calculating the mean and standard error of the energy between tubulins and CFAP52 from the entire trajectory, the energy of the acetylated αK40 case is only slightly lower than that of the non-acetylated αK40 case (Fig. 5D). Similarly, no difference between acetylated and non-acetylated αK40 in interactions with similar setup using RIB72A. Even when accounted for the periodic structures of DMT with many MIPs, the energy difference between acetylated and non-acetylated αK40 with MIPs is still not significant.

Our coarse-grain molecular dynamic simulations of MIPs and αK40 suggest that acetylation likely does not play a role in the interaction with MIPs.

Mass spectrometry reveals changes in DMT protein composition in response to a lack of αK40 acetylation

Our analysis thus far has failed to reveal significant structural differences in the MIPs within the DMT structures of *WT*, *K40R* and *MEC17-KO* mutants. Therefore, we searched for more subtle changes in the axoneme composition using mass spectrometry. We analyzed the same DMT samples used for cryo-EM, which contain no membrane and matrix fractions, to see any proteomic changes due to the lack of acetylation. In addition, to eliminate the downstream effect of the lack of acetylation i.e. destabilization of DMT, we combined the mass spectrometry results in this study with the mass spectrometry studies of the *RIB72A/B-KO* and *RIB72B-KO* mutants (S. Kubo et al., 2023). The *RIB72A/B-KO* mutant lacks both RIB72A and RIB72B, which leads to a significant number of MIPs missing and slower swimming speed (Stoddard et al., 2018). Therefore, we can use *RIB72B-KO* and *RIB72A/B-KO* as controls to specifically look for the upstream effect due to the lack of acetylation.

We first performed a control of proteins not supposed to interact with αK40 by analyzing the levels of radial spoke proteins and found no significant differences (Fig. S4A). We then looked at the MIP abundance. Most MIPs showed no significant changes in their abundance (less than 1.5-fold changes) except for CFAP112, CFAP141 and RIB27 (Fig. 6A) in the *K40R* and *MEC17-KO* samples. However, we did not observe any differences in the periodicity of CFAP112, CFAP141 and RIB27 in the cryo-EM maps of the DMTs from *WT*, *K40R* and *MEC17-KO* mutants. As shown recently in the case of CFAP77A and CFAP77B, certain MIPs might not localize consistently along the length of the

cilium (S. Kubo et al., 2023), and there might be some changes in the occupancy of those MIPs in a specific region that lead to changes in their abundance.

There were 11 proteins significantly elevated in both *K40R* and *MEC17-KO* mutants by fourfold compared to the wild type (Fig. 6B, Fig. S4B, C). One of these proteins was also elevated in the *RIB72A/B-KO* mutant vs. *WT*, and therefore, 10 proteins were specifically upregulated in both the *K40R* and *MEC17-KO* strains (Fig. 6B, G). Similarly, we found that three proteins were significantly reduced in both *K40R* and *MEC17-KO* but not in the *RIB72A/B-KO* knockout mutant (Fig. 6C, E). Among the proteins reduced or missing in the *K40R* and *MEC17-KO* mutants, there are protein phosphatase 2A-related proteins: PP2A regulatory subunit A (TTHERM_00766530, UniProt ID: I7MAR7), PP2C (TTHERM_00316330, UniProt ID: I7LW71), and PP2A (TTHERM_00355160, UniProt ID: Q22Y55) (Fig. 6D). Furthermore, one kinase was downregulated in *MEC17-KO* and *K40R* cells (Fig. 6E) (TTHERM_00623090, UniProt ID: Q240X5). In *Chlamydomonas*, PP2A is present in DMT and required for normal ciliary motility (Elam et al., 2011). It was previously reported that the knockdown of PPP1R2 (protein phosphatase inhibitor 2) reduces αK40-acetylation in the primary cilium of human retinal epithelial cells (Wang & Brautigan, 2008). Inhibition of protein phosphatase (1 and 2A) with calyculin in PPP1R2 knockdown cells partially rescued the acetylation of ciliary microtubules. These results suggest that the lack of αK40 acetylation reduces PP2A activity in DMT. Therefore, we can infer that acetylation and phosphorylation interact in DMT.

DISCUSSION

In this work, we reinforced the notion that acetylation of αK40 makes the loop less flexible (Eshun-Wilson et al., 2019) by molecular dynamics. In addition, we performed structural characterization of the DMTs from two acetylation mutants, *K40R* and *MEC17-KO,* and compared them to that of the wild type. We showed that the αK40 loops are structured when they interact with MIPs and identified DM10 as an αK40 interacting domain. This suggests that the αK40 loop plays an important role in certain MIP-tubulin interactions. On the other hand, the αK40 loop-MIP interactions do not detectably change their structures between acetylated and non-acetylated αK40. These results imply that a complete DMT with MIPs is assembled without the need of acetylation. Later, the MEC17/ATAT1 acetyltransferase acetylates αK40.

Interestingly, we observed significant changes in inter-PF angles in the B-tubule, where MIPs are fewer. Our results suggest that αK40 loop interactions with MIPs are the dominant interactions that stabilize microtubules regardless of acetylation status. When there are fewer MIPs and thus less interaction between the αK40 loop and MIPs, the contribution of the acetylation of αK40 to the lateral interaction between adjacent PFs becomes more significant (Fig. 7). As a result, the lack of acetylation destabilizes DMT and leads to tubulin lattice alteration and instability. In a recent study (Viar, Klena, Martino, Nievergelt, & Pigino, 2023), the tip region of the Chlamydomonas cilia is acetylated early during growth compared to other PTM such as polyglutamylation and polyglycylation. In the tip, the microtubules exist as singlet microtubules and do not have regular MIP binding pattern like in the base region (Legal et al., 2023). As a result,

acetylation might play an essential role in the ciliary tip region to stabilize microtubules. Moreover, our study supports the notion that acetylation of tubulin is not a biphasic switch but a fine-tuning mechanism that impacts microtubule stability. Our results again demonstrate that the tubulin lattice can be a read-out for DMT stability (Ichikawa et al., 2019). Recently, it has been shown that acetylation of K394, which is located at the αβ-tubulin dimer interface, is specific to flies' nervous system and is critical to neuronal growth (Saunders et al., 2022). This finding might suggest that different acetylation sites can be fine-tuned for different purposes. Interestingly, cryo-ET and fluorescence data showing that acetylation signals appears very early at the ciliary tip during ciliary assembly (Viar et al., 2023). Logically, this is consistent with our findings because not a lot of MIPs are assembled at the tip of the cilia, so acetylation is maintaining the structural integrity here.

Since both acetylation mutants lack protein phosphatase 2A and its regulatory subunits, there could be an interaction between tubulin acetylation and protein phosphatase 2A in cilia. TGF-β-activated kinase 1 (TAK1) is an important activator of αTAT1 in mice (Shah et al., 2018). We can speculate that the absence of αK40 acetylation could also affect the enzyme MEC17/ATAT1 and its availability for phosphorylation by TAK1 or other kinases. Possibly, the lack of αK40 acetylation changes the phosphorylation levels by altering the balance between kinases and phosphatases (protein phosphatase 2A in this case). Interestingly, HDAC6 deacetylase is also regulated by multiple kinases (Du, Seibenhener, Yan, Jiang, & Wooten, 2015). This again highlights the interdependence of phosphorylation and acetylation in cilia. Furthermore, crosstalk occurs between αK40

acetylation and other tubulin PTMs, namely polymodification. For example, *Tetrahymena* mutants lacking tubulin polyglycylases (TTLL3) have elevated levels of αK40 acetylation (Wloga, Webster, et al., 2009). Our mass spectrometry results showed that a tetratricopeptide repeat protein (TTHERM_00313720, UniProt ID: Q22KA9) was downregulated in *MEC17-KO* and *K40R* mutants (Fig. 6E). Protein BLAST found a homolog in *Homo sapiens* as tetratricopeptide repeat protein 30B/IFT70 (UniProt ID: Q8N4P2), an IFT protein whose depletion reduces polyglutamylation of axonemal tubulin (Pathak, Obara, Mangos, Liu, & Drummond, 2007). We also observed that the absence of αK40 acetylation affects the PF angles and the impact is stronger on the B-tubule. The B-tubule is enriched in polymodification (polyglutamylation and polyglycylation), and therefore, the altered B-tubule structure could affect the access of enzymes that add or remove polymodification. In fact, some of the effects of the absence of αK40 acetylation based on the use of non-acetylated axonemes (Reed et al 2006) could be due to alterations of the B-tubule, namely, the levels of polymodification. Together with our results and others (Akella et al., 2010; T. Kubo et al., 2015; Rogowski et al., 2010b; Wloga, Dm, et al., 2009; Wloga et al., 2008), these results suggest that the PTM in cilia is in a balancing act. Changing one type of PTM can shift the balance of other types of PTMs.

MATERIALS AND METHODS

Growth of *Tetrahymena* cells for isolation

Bean media (Williams, Wolfe, & Bleyman, 1980) was used to store *Tetrahymena* cells (*WT (CU428), K40R, MEC17-KO*), with 4 µL of the cell culture transferred into 40 mL of liquid SPP media (Gorovsky, Yao, Keevert, & Pleger, 1975). The cells were grown for 7 days at room temperature and then transferred into 50 mL of SPP liquid media overnight growth at 30°C with 150 RPM shaking in a Thermo Fisher MAXQ8000 incubator. Then, 50 mL of this overnight culture was added to 900 mL of liquid SPP media and grown at 30°C (MAXQ8000) at 150 RPM for two days or until the OD_{600} was 0.7.

Flagella isolation via dibucaine treatment

To harvest *Tetrahymena* cells, overnight culture was centrifuged at 700 × g for 10 minutes with slow deceleration at 22°C in an Avanti Centrifuge (Rotor JLA-8.1000). Ten milliliters of room temperature SPP medium supplemented with DTT was used to resuspend the cell pellet and then adjusted to a final volume of 24 mL, followed by transfer to an ice-cold 250 mL Erlenmeyer flask. Immediately, 1 mL of dibucaine (dissolved in distilled water at 25 mg/mL) was added to the flask and gently swirled for exactly 60 seconds in an ice water bath. To stop the reaction, 75 mL of ice-cold SPP media (supplemented with 1 mM EGTA) was immediately added to the Erlenmeyer flask and then split into two 50 mL conical tubes for centrifugation at 2000 × g for 10

minutes at 4°C with no deceleration (Sorvall ST 16R, Rotor 75003181). The supernatant that contained cilia was transferred to centrifuge tubes for the Beckman Coulter JA 25.50 rotor, approximately 30 mL per tube, for centrifugation at 17000 × g for 40 minutes at 4°C with slow deceleration (Avanti, Rotor JA25.50). The pellet was gently washed with Cilia Wash Buffer (50 mM HEPES at pH 7.4, 3 mM MgSO4, 0.1 mM EGTA, 1 mM DTT, 250 mM sucrose). and frozen with liquid nitrogen for storage in a -80°C freezer.

Purification of DMT fraction

The cilia suspension was thawed on ice and then centrifuged at 16000 g and 4°C for 10 minutes in a microfuge in a refrigerated room (Eppendorf, Centrifuge 5415 D). The pellet was resuspended in 250 µl of ice-cold Cilia Final Buffer (50 mM HEPES at pH 7.4, 3 mM MgSO4, 0.1 mM EGTA, 1 mM DTT, 0.5% trehalose, 1 mM PMSF). To clean the cilia, the resuspended cilia were centrifuged at 16000 × g for 10 minutes at 4°C in a microfuge (Eppendorf, Centrifuge 5415 D), and the supernatant was removed. Then, the pellet was resuspended in 250 µl of Cilia Final Buffer [without trehalose but with 44.1 µl of 10% NP-40 alternative (Millipore Sigma, 492016)] added to a final concentration of 1.5% NP-40]. The sample was placed on ice to incubate for 30 minutes before the demembraned flagella supernatant was removed after centrifugation at 16,000 × g for 10 min at 4°C in a microfuge (Eppendorf, Centrifuge 5415 D). The pellet containing the axoneme was resuspended in 245 µl of Cilia Final Buffer (without trehalose), and then 2.5 µl of 100 mM ADP (to a final concentration of 1 mM ADP) was added for incubation at room temperature for 10 minutes. This was followed by adding

2.5 µl of 10 mM ATP (to a final concentration of 1 mM ATP) for incubation at room temperature for 10 minutes. Bradford reagent (Bio-Rad 5000201) was used to measure the total protein concentration, and the final protein concentration was adjusted to 3 mg/mL using Cilia Final Buffer (without trehalose).

Cryo-EM sample preparation

The concentration of the DMT solution was adjusted to 3 mg/ml. Quantifoil R2/2 grids (Electron Microscopy Sciences, #Q225CR-06) were treated using 1 mL of chloroform overnight followed by negative glow discharge (30 seconds at 25 mAh). Then, 3.5 µl of axoneme sample was applied to treated grids inside the Vitrobot Mark IV (Thermo Fisher) at a blot force of 3, blot time of 5 seconds, and drain time of 0.5 seconds, followed by plunge freezing into liquid ethane.

Cryo-EM data acquisition

Using a Titan Krios 300 kV FEG electron microscope (Thermo Fisher) with a K3 Summit direct electron detector (Gatan, Inc.) and the BioQuantum energy filter (Gatan, Inc.), movies of the axoneme were acquired at 64kx nominal magnification (calculated pixel size of 1.370 Å/pixel) using SerialEM (Mastronarde, 2005). A total dose of 45 electrons per $Å^2$ over 40 frames for the *WT* and *MEC17-KO* datasets. A total dose of 73 electrons per $Å^2$ per frame over 30 frames for the *K40R* dataset. The defocus range was between -1.0 and -3.0 µm at an interval of 0.25 µm.

Cryo-EM image processing

Motion correction and dose-weighting of the movies were performed using MotionCor2 (Zhang et al., 2017) implemented in Relion 3 (Zivanov et al., 2018), and the contrast transfer function parameters were estimated using Gctf (Zhang, 2016). Micrographs with apparent drift, ice contamination, and poor contrast transfer function estimation were discarded (18384, 25610, 4283 micrographs for *WT, K40R* and *MEC17-KO* data, respectively). The filaments were picked manually using e2helixboxer (Tang et al., 2007).

An 8-nm periodicity was used to pick particles of 512 x 512 pixels, binned twice, and prealigned using a modified version of the Iterative Helical Real Space Reconstruction script (Egelman, 2007) in SPIDER (Frank et al., 1996) to work with nonhelical symmetry. The alignment parameters were then transferred to Frealign to align the particles for 6 iterations in Frealign (Grigorieff, 2007) and then converted into Relion 3.0. In Relion 3, iterative per-particle-defocus refinement and Bayesian polishing were performed for the 80 nm particles.

Particles were subtracted from their tubulin lattice signal and underwent 3D classification into two classes to obtain the 16-nm repeat particles. The 16-nm repeat particles were then subjected to 3D classification into 3 classes to obtain the 48-nm repeat particles. The 48-nm particles were then refined, resulting in resolutions of 3.5 and 4.3 Angstrom for *K40R* and *MEC17-KO* DMTs from 182387 and 39417 particles, respectively.

To improve the local resolution for each PF during modeling, we performed focused refinements by using masks to cover adjacent PF regions in the DMT. Next, the maps were enhanced by DeepEmhancer (Sanchez-Garcia et al., 2021) to improve visualization and interpretability.

Tubulin Modeling

The WT tubulin model 6U0H (Ichikawa et al., 2019) was first fitted into the higher-resolution *K40R* cryo-EM map and then locally modeled using Coot (Emsley et al, 2010) and real space refined in Phenix (Adams et al, 2010) for generation of the *K40R* tubulin model. The *WT* and *MEC17-KO* tubulin models were generated by fitting the *K40R* tubulin model in *WT* and *MEC17-KO* cryo-EM maps, respectively, followed by refinement in Coot (Emsley et al, 2010) and Phenix (Adams et al, 2010). The αK40 loop regions from *WT*, *K40R*, and *MEC17-KO* were locally modeled in focused refinement cryo-EM maps using Coot (Emsley et al, 2010) and Phenix (Adams et al, 2010). All the maps and model visualization were taken using ChimeraX (Goddard et al., 2018).

Coarse-grained molecular dynamic simulation.

Based on the atomic structures of the four tubulin dimers, CFAP52 and IJ34, we performed coarse-grained molecular dynamic simulations. The purpose of this simulation was to check the effect of acetylated αK40 on the binding stability of CFAP52. In the coarse-grained model, each amino acid was represented as a single bead located at its Cα position. To observe their dynamics, we used the excluded volume

effect, electrostatic interaction, and the energy function AICG2+ (Li, Terakawa, Wang, & Takada, 2012; Li, Wang, & Takada, 2014). In AICG2+, the reference structure was assumed to be the most stable conformation, and their parameters were modified from the reference. It is known that the intradimer interaction is much stronger than the interdimer interaction, and the interdimer interaction is much stronger than the intra-PF interaction, so we set the interdimer and PFs' nonlocal native interaction force to 0.8 and 0.3 times the original value, respectively, while that of the intradimer was kept as the original value (1.0 times). Of note, three residues (PHE133, GLY308, and GLU401) of the B9-PF beta-tubulin at the plus end side were anchored in their position for convenience analysis. We performed the simulation 10 times with acetylated αK40 and non-acetylated αK40 structures using the CafeMol package version 2.1 (Kenzaki et al., 2011). Each molecular dynamic simulation took 3×10^7 molecular dynamic steps, and they were conducted by the underdamped Langevin dynamics at 300 K temperature. We set the friction coefficient to 0.02 (CafeMol unit), and default values were used for others.

Normally, in dealing with electrostatic interactions, LYS and ARG, GLU and ASP, and other amino acids were given a charge of +1, -1, and 0, respectively. However, in this simulation, it was necessary to evaluate the electrostatic interaction as accurately as possible, so we calculated the surface charge density from the all-atom structure and remapped the charge distribution using only Ca beads to reproduce the all-atom surface charge distribution. The technique is called RESPAC (Terakawa & Takada, 2014). We applied RESPAC to regions without missing data, such as the αK40-loop and E-hook.

For the missing region (and so we performed loop modeling by MODELLER (Šali & Blundell, 1993), we treat their charge by default definition. In the coarse-grained model, each amino acid is treated as a single bead, so we simply assumed that if αK40 was acetylated, its charge was zero, while non-acetylated αK40 had a +1 charge.

All-atom molecular dynamic simulation.

The purpose of the all-atom molecular dynamic simulation was to check whether the acetylated αK40 loop takes fewer conformations than the non-acetylated αK40 loop. In the all-atom molecular dynamic simulation using GROMACS (Abraham et al., 2015; Pronk et al., 2013), we used the GROMOS54a7 force field for protein (Schmid et al., 2011) and SPC for solvent water (Jorgensen & Tirado-Rives, 2005). We added sodium and chloride ions to neutralize the system and to make the salt concentration approximately equal to 0.1 Energy minimization by the steepest descent minimization algorithm was followed by equilibration with NVT and NPT for 100 ps at 300 K. In the production run, we used NPT ensemble simulations with 1 atm and 300 K. The production run consisted of a 1 fs step for 180 ns. The α-tubulin at the plus end of B9-PF was used as a reference structure for the simulation. To model the structure of acetylated αK40, Vienna-PTM 2.0 was used (Margreitter, Petrov, & Zagrovic, 2013; Margreitter, Reif, & Oostenbrink, 2017; Petrov, Margreitter, Grandits, Oostenbrink, & Zagrovic, 2013). The force field used (GROMOS54a7) had already been set up for the acetylated lysine.

Measurement of inter-PF rotation angles.

The inter-PF rotation angle can be defined by the lateral rotation angle between each subsequent PF pair. The rotation angles and Z-shift between PF pairs were measured using the “measure” command from ChimeraX (Pettersen et al., 2004). Data for *WT, K40R*, and *MEC17-KO* cells were compiled into GraphPad Prism 9 to perform ANOVA and plotting.

Measurement of interdimer distance.

We docked in the atomic models of the α- and β-tubulins in the maps of *WT, K40R*, and *MEC17-KO*. The interdimer distance was measured between the N9 GTP of α-tubulin and that of the next α-tubulin in the same PF using the “distance” command from Chimera (Pettersen et al., 2004).

Mass Spectrometry

Samples prepared for cryo-EM were used for mass spectrometry analysis. Laemmli buffer at 4X (#1610747, Bio-Rad) was added to the microtubule fraction samples in Cilia Final Buffer buffer so that it was 1x, and 25-30 µg protein was loaded on the SDS□PAGE gel. Electrophoresis was performed, but the run was terminated before the proteins entered the separation gel. A band containing all proteins in the sample was then cut out from the gel and subjected to in-gel digestion. The obtained peptides (~2 µg) were chromatographically separated on a Dionex Ultimate 3000 UHPLC. First, peptides were loaded onto a Thermo Acclaim Pepmap (Thermo, 75 µm ID × 2 cm with 3

μm C18 beads) precolumn and then onto an Acclaim Pepmap Easyspray (Thermo, 75 μm × 25 cm with 2 μm C18 beads) analytical column and separated with a flow rate of 200 nl/min with a gradient of 2-35% solvent (acetonitrile containing 0.1% formic acid) over 2 hours. Peptides of charge 2+ or higher were recorded using a Thermo Orbitrap Fusion mass spectrometer operating at 120,000 resolution (FWHM in MS1, 15,000 for MS/MS). The data were searched against the *Tetrahymena thermophila* protein dataset from UniProt (https://www.uniprot.org/).

Mass spectrometry data were analyzed by Scaffold_4.8.4 (Proteome Software Inc.). Proteins with mean values of exclusive unique peptide count of 2 or more in the WT mass spectrometry results were used for analysis. Raw mass spectrometry data were normalized by the total spectra. ANOVA statistical tests were applied to *MEC17-KO*, *K40R* and *WT* mass spectrometry results using biological triplicates. Proteins exhibiting a minimum of twofold increase/decrease and a statistical significance threshold ($p < 0.05$) in mutants compared to *WT* were identified as up- or downregulated.

Data availability

The data produced in this study are available in the following databases:

・Cryo-EM maps of the 48-nm repeat of *MEC17-KO* DMT: EMDB EMD-40436

・Model coordinates of the *MEC17-KO* DMT: PDB 8SF7

The WT and K40R structures used in this paper have associated maps in the Electron Microscopy Data Bank database with the following EMDB IDs EMD-29685 and EMD-29692.

The WT and K40R structures used in this paper have coordinates in the RCSB Protein Data Bank database with the following PDB IDs 8G2Z and 8G3D.

Acknowledgments

We thank Drs. Kelly Sears, Mike Strauss, Kaustuv Basu, and Jeannie Mui (Facility for Electron Microscopy Research at McGill University) for helping with data collection and maintenance of the electron microscopes. We thank Amy Wong, Lorne Taylor and Jean-François Trempe (RI-MUHC Proteomics Platform) for their help with mass spectrometry. SK is supported by a JSPS Overseas Research Fellowship. KHB is supported by grants from the Canadian Institutes of Health Research (PJT-156354) and Natural Sciences and Engineering Research Council of Canada (RGPIN-2022-04774). JG is supported by NIH grants R01GM135444 and R01GM139856, respectively.

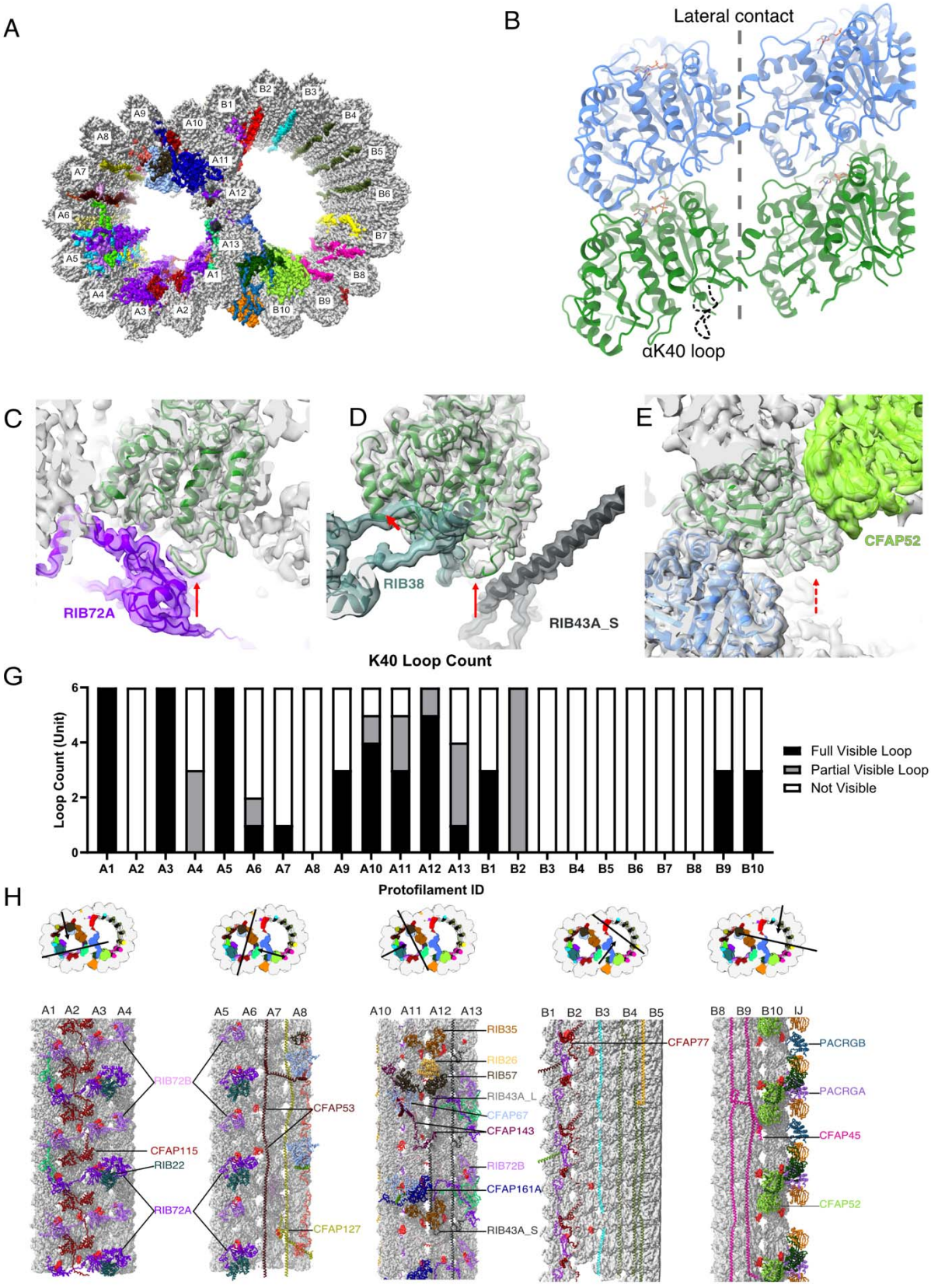
A
B
Lateral contact
αK40 loop
C
RIB72A
D
RIB38
RIB43A_S
E
CFAP52
G
K40 Loop Count
Loop Count (Unit)
Full Visible Loop
Partial Visible Loop
Not Visible
Protofilament ID
H
RIB72B
CFAP115
RIB22
RIB72A
CFAP53
CFAP127
RIB35
RIB26
RIB57
RIB43A_L
CFAP67
CFAP143
RIB72B
CFAP161A
RIB43A_S
CFAP77
PACRGB
PACRGA
CFAP45
CFAP52

Figure 1. The presence of the structure αK40 loop in *Tetrahymena thermophila* DMT. (A) Surface rendering of the DMT viewed from the tip of the cilia, with MIPs colored in the 48-nm repeat cryo-EM electron density map of *Tetrahymena*. (B) Relative location of the αK40 loop (dashed black line) and the lateral contacts of tubulins. Color: α-tubulin, green; β-tubulin: blue. (C-F) Cryo-EM map and models of the fully structured αK40 loops in PF A3 (C-D) and the fully structured (E) and partially structured (F) αK40 loops in PF B10. The red arrows point to the location of the αK40 loops. (G) Bar graph showing the composition of visible full (missing no more than two residues from residues 37 to 48) and partial loops (missing 3-5 residues) in both the A- and B-tubules. (H) 48-nm repeat surface rendering of selected PFs with MIPs that interact with visible full and partial αK40 loops colored in red, indicating that αK40 loops are structured in regions with many MIPs.

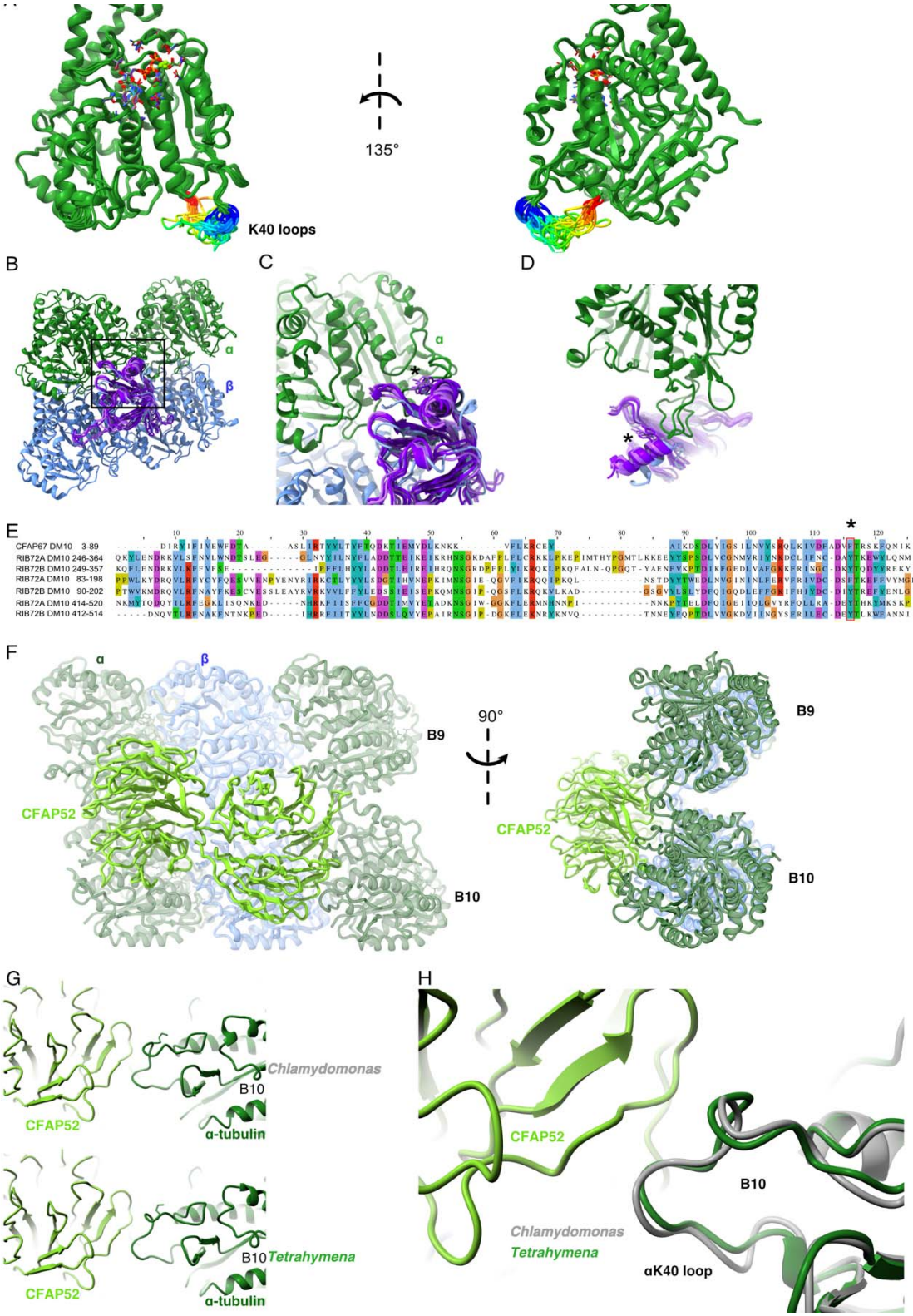

Figure 2: Comparison of αK40 loop conformation.

(A) Superimposed view of all the orientations of all the visible full and partial αK40 loops, showing their orientation. (B) Interaction of K40 loop and DM10 domains from RIB72A (3 domains, blue), RIB72B (3 domains, purple) and CFAP67 (1 domain, cyan). Black

box represents the view in (C). (C) Zoom in view of DM10 domains and K40 loop interaction. Asterisk (*) denotes the conserved aromatic residue potentially interact with the K40 loop. (D) Alternative view of DM10 domains interacting with K40 loop. (E) Multiple sequence alignment of DM10 domains from RIB72A, RIB72B and CFAP67. (F) Cryo-EM map (left) and model (right) of the inner junction region of *Tetrahymena* to show the interaction of the full αK40 loop with CFAP52. (G) Cryo-EM map (left) and model (right) of the inner junction region of *Chlamydomonas* to show the interaction of the full αK40 loop with CFAP52. (H) Superimposed view of the *Chlamydomonas* αK40 loop (gray) onto the *Tetrahymena* αK40 loop of B10.

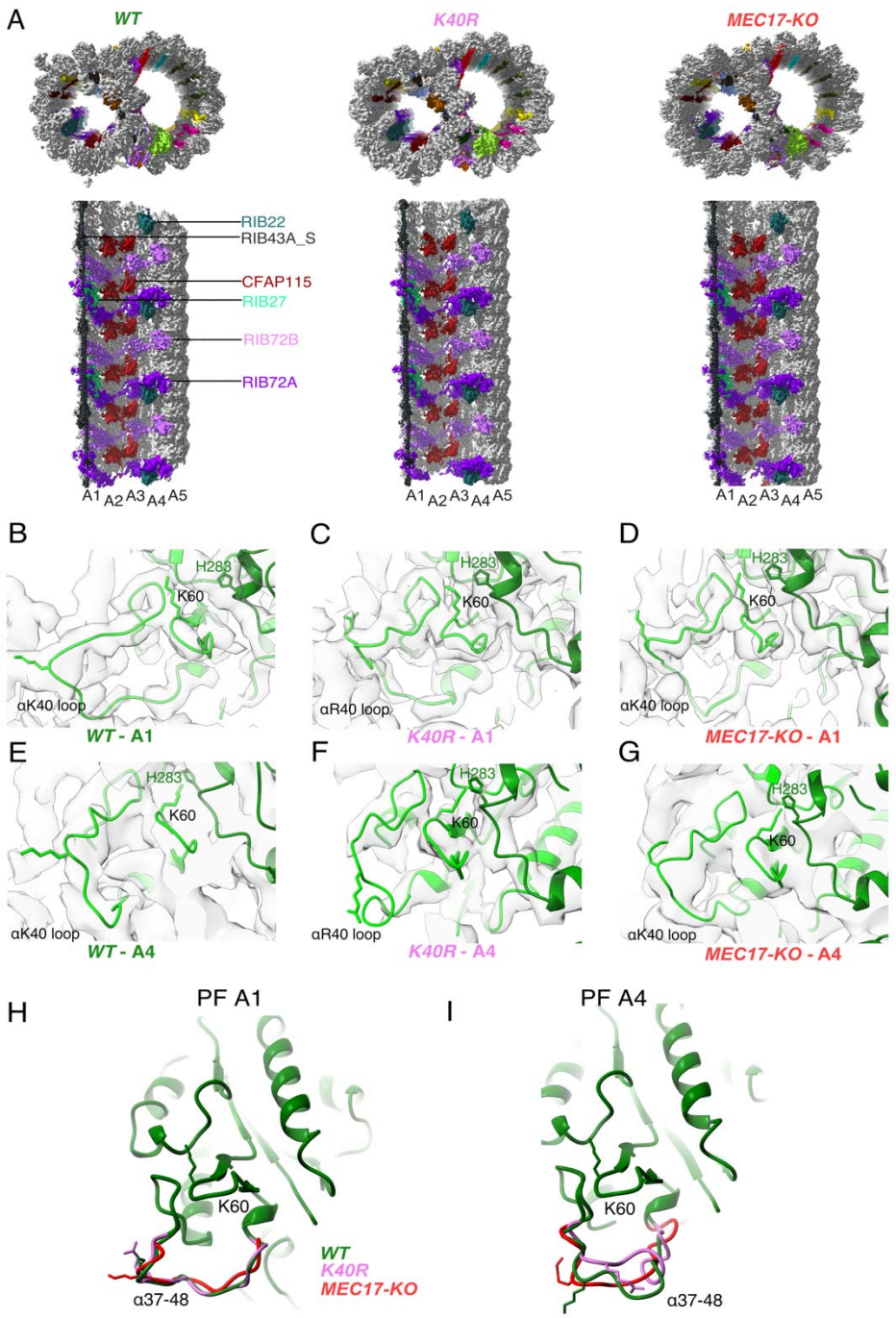

Figure 3: Comparison of DMT structures from *WT*, *MEC17-KO* and *K40R* mutants
(A) Comparison of the cryo-EM density maps of the DMT from *WT*, *K40R*, and *MEC17-KO* strains of *Tetrahymena* to show that the MIPs are intact in all three species. (B-G). Models of the full αK40 loops in PF A1 (B-D) and PF A4 (E-G) from *WT*, *K40R*, and *MEC17-KO* strains. (H-I) Models of the αK40 loops from A1 (H) and A4 (I) superimposed from *WT*, *K40R*, and *MEC17-KO* species.

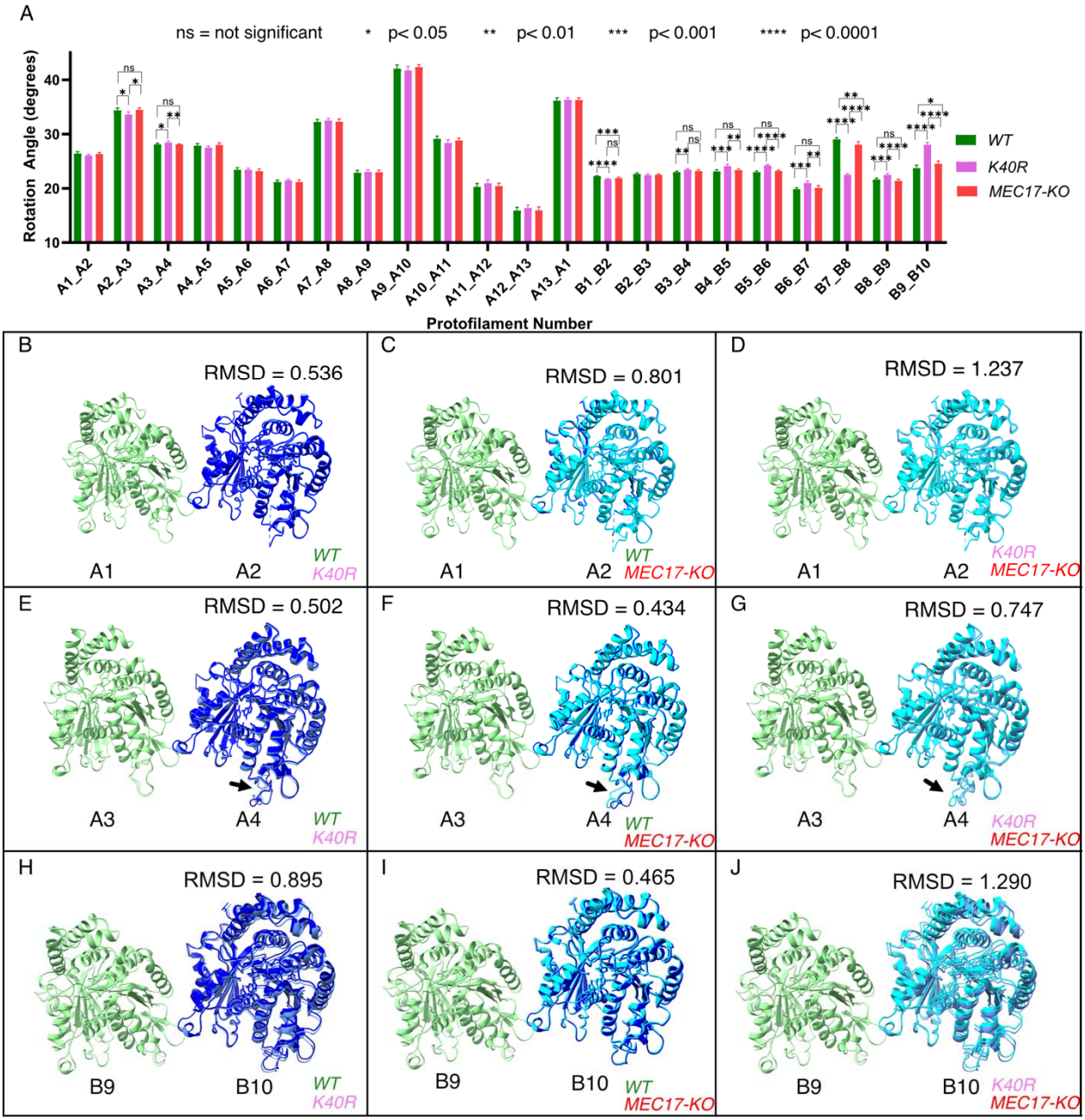

Figure 4: Deacetylation affects the inter-PF angles in the DMT.
(A) Rotation angles for each PF across all three strains (*WT, K40R, MEC17-KO*). (B-D) Comparison of rotation angle change between A1 and A2, showing minor changes. (E-G) Comparison of rotation angle change between A3 and A4, showing minimal changes. Red arrows point to the changes in αK40 loop shape between each species. (H-J) Comparison of rotation angle change between B9 and B10, showing significant changes.

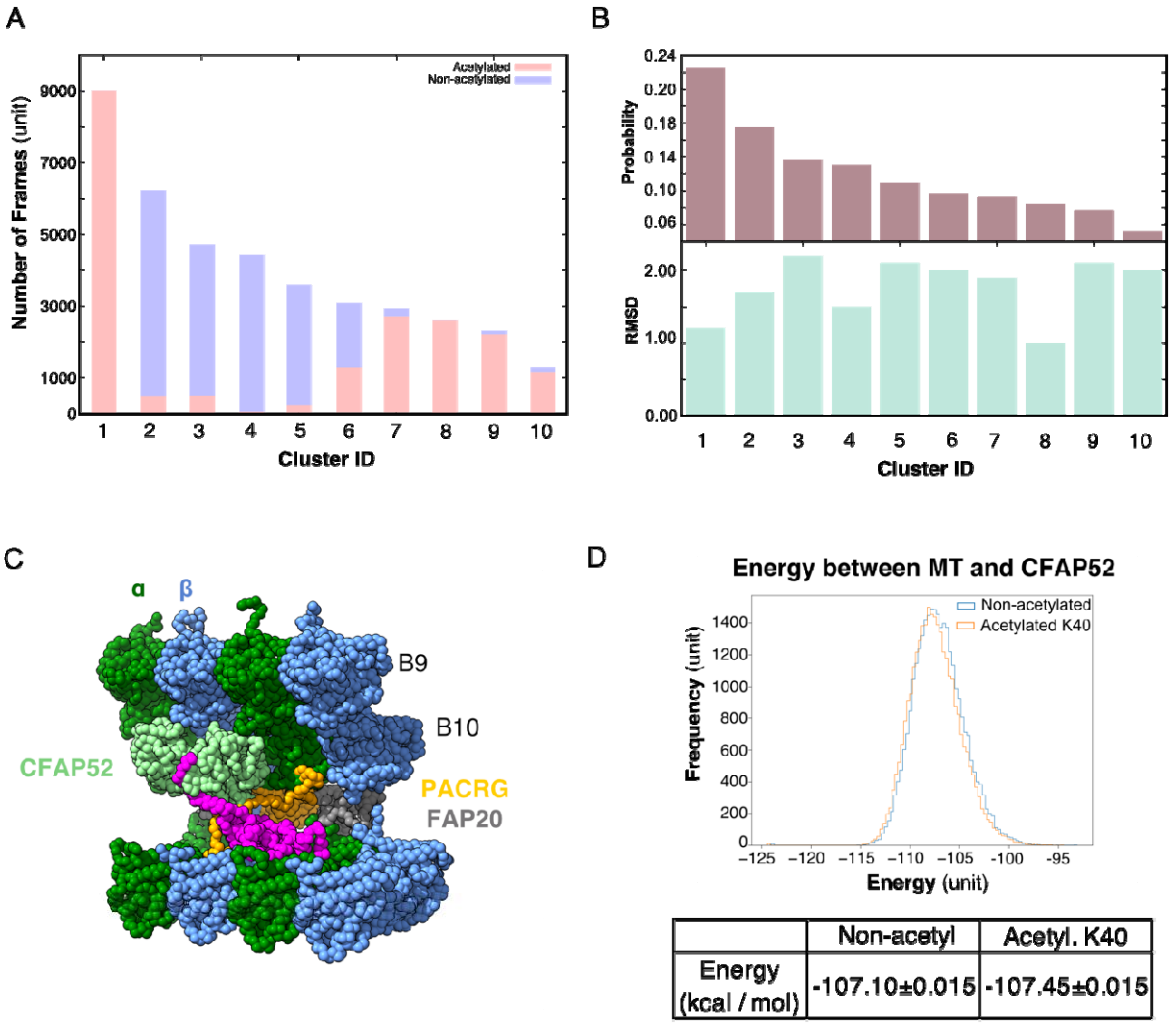

	Non-acetyl	Acetyl. K40
Energy (kcal / mol)	-107.10±0.015	-107.45±0.015

Figure 5. Molecular dynamic simulations of the acetylated and non-acetylated αK40 loops.

(A) All-atom simulations of αK40 loop clusters in different conformations of acetylated (pink) and base/non-acetylated (blue) indicate that acetylated conformations adopt higher frames and are less flexible. (B) RMSD and probability of each cluster simulated in A. (C) Molecular dynamics coarse grain model of the inner junction region of *Tetrahymena*; each amino acid is 1 bead. (D) Graph showing the energy difference (in kcal/mol) between base (non-acetylated) and acetylated αK40 to show that each acetylated αK40 has slightly lower energy than the non-acetylated αK40.

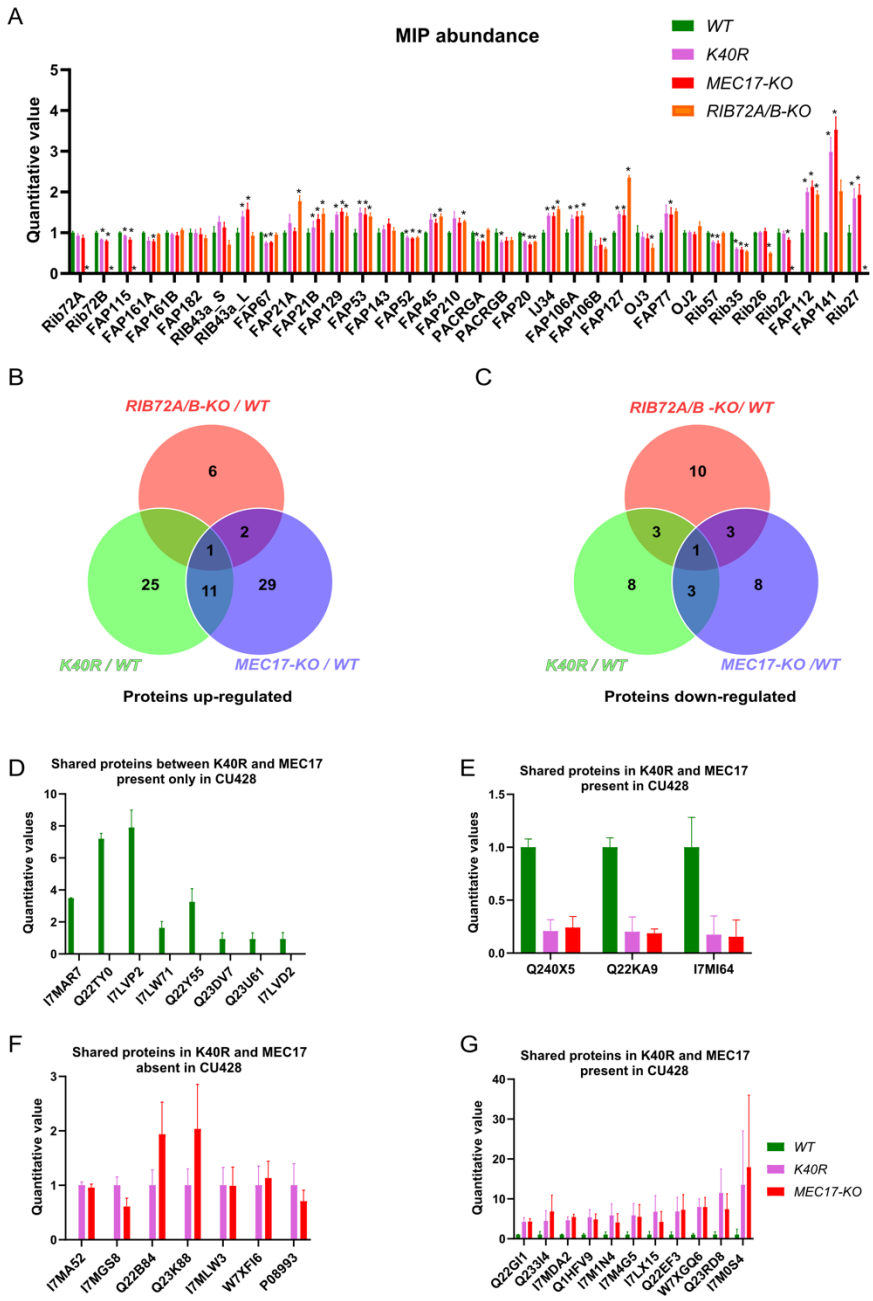

Figure 6. Mass spectrometry of *WT, K40R* and *MEC17-KO* mutants.
(A) Bar graph showing the abundance of MIPs based upon quantitative values (normalized total spectra) from mass spectrometry. Asterisk (*) indicates a significant difference with $p < 0.05$. (B) Proteins upregulated in *RIB72A/B*, *K40R*, and *MEC17-KO* mutants compared with the *WT*. (C) Proteins downregulated in *RIB72A/B, K40R*, and *MEC17-KO* mutants compared to the *WT.* (D) Proteins only found in the mass spectrometry of *WT* when compared with *K40R* and *MEC17-KO* mutants. (E) Downregulated proteins in both *K40R* and *MEC17-KO* mutants compared to *WT*. (F) F. Proteins in both *K40R* and *MEC17-KO* mutants but are absent in *WT.* (G) Upregulated proteins in both *K40R* and *MEC17-KO* mutants compared to *WT*.

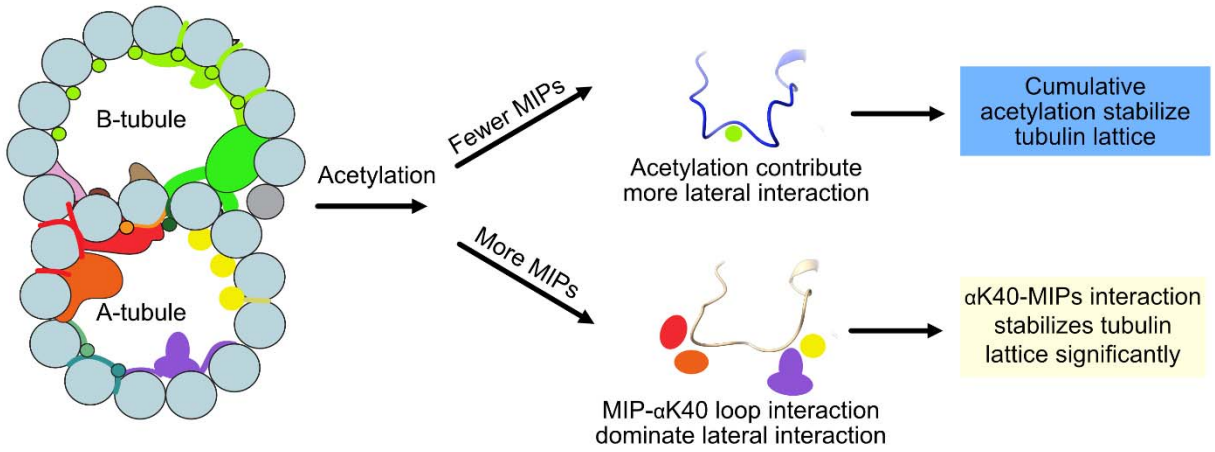

Figure 7: Models of acetylation contribution in the DMT

In the case of more MIPs, such as in the A-tubule, the MIP-αK40 interaction dominates the contribution to the lateral interaction; therefore, deacetylation does not affect the structures significantly. With fewer MIPs, such as in the B-tubule, acetylation contribution to the lateral interaction becomes significant and therefore can contribute to the stabilization of the tubulin lattice.

Table 1: Cryo-EM data collection refinement

	WT (CU428)	***K40R***	***MEC17***
Data collection & Processing			
Microscope	Titan Krios	Titan Krios	Titan Krios
Electron Detector	Gatan K3	Gatan K3	Gatan K3
Zero-loss filter (eV)	30	30	30
Magnification	64,000	64,000	64,000
Voltage	300	300	300
Electron exposure	45 e/A^2	45 & 73 e/A^2	45 e/A^2
Defocus range	1.0-3.0 µm	1.0-3.0 µm	1.0-3.0 µm
Pixel size	1.37	1.37	1.37
Symmetry imposed	C1	C1	C1
Movies acquired	18,384	25610	4283
Particles number	148365	182355	39417
Map resolution (Å)	3.6 – 4.0	3.3 – 3.5	4.0-4.5

Table 2: Refinement statistics of WT, K40R and MEC17 48nm models.

	WT (CU428)	***K40R***	***MEC17***
Model-to-Map fit, CCmask	0.8009	0.7961	0.6070
All-atom clashscore	16.61	13.21	57.06
Ramachandran plot **Outliers [%]** **Allowed [%]** **Favored [%]**	 0.14 3.70 96.16	 0.14 3.60 96.26	 0.14 6.13 93.73
Rotamer outliers [%]	0.03	0.04	0.02
Cbeta deviations [%]	0.00	0.00	0.01
Cis-proline [%]	4.56	4.56	4.54
Cis-general [%]	0.01	0.01	0.03
Twisted proline [%]	0.17	0.18	0.13
Twisted general [%]	0.02	0.01	0.02

Supplementary Figures and Tables

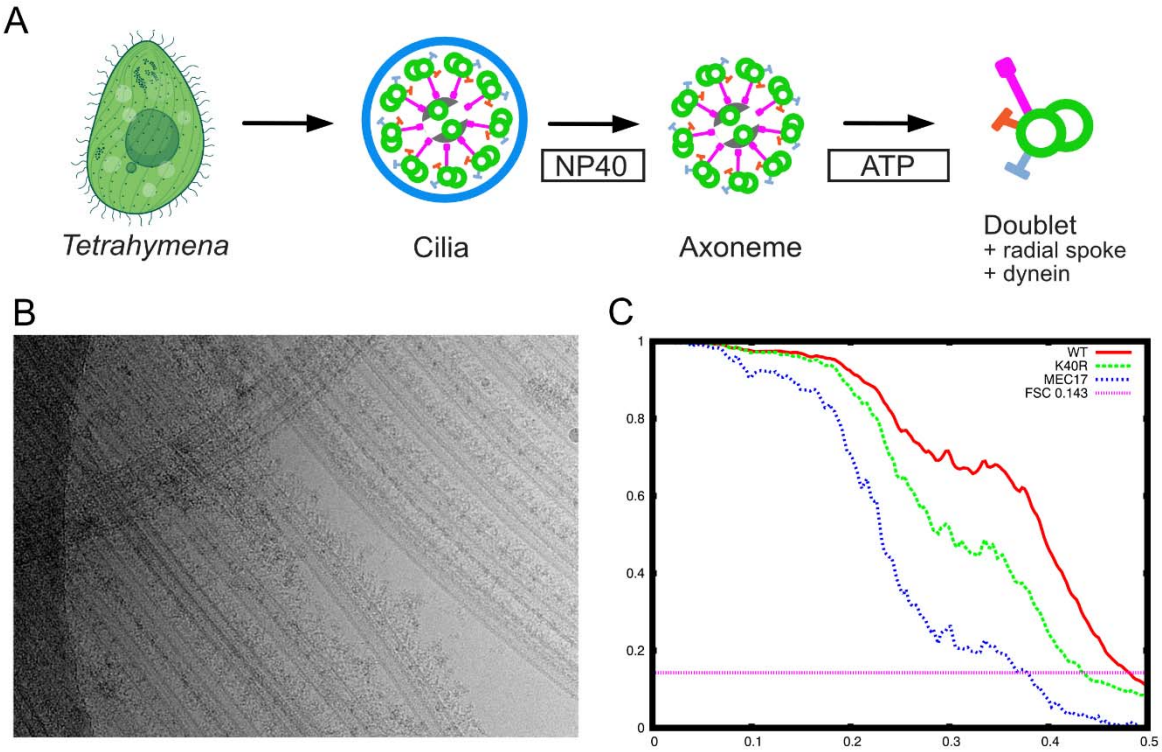

Figure S1. Purification and structure determination of DMT.
(A) Purification scheme of the axoneme in this study. (B) A typical cryo-EM image of the *Tetrahymena* DMT. (C) Gold-standard Fourier shell correlation of the 48-nm repeat cryo-EM maps of the *WT, K40R, and MEC17-KO Tetrahymena* strains.

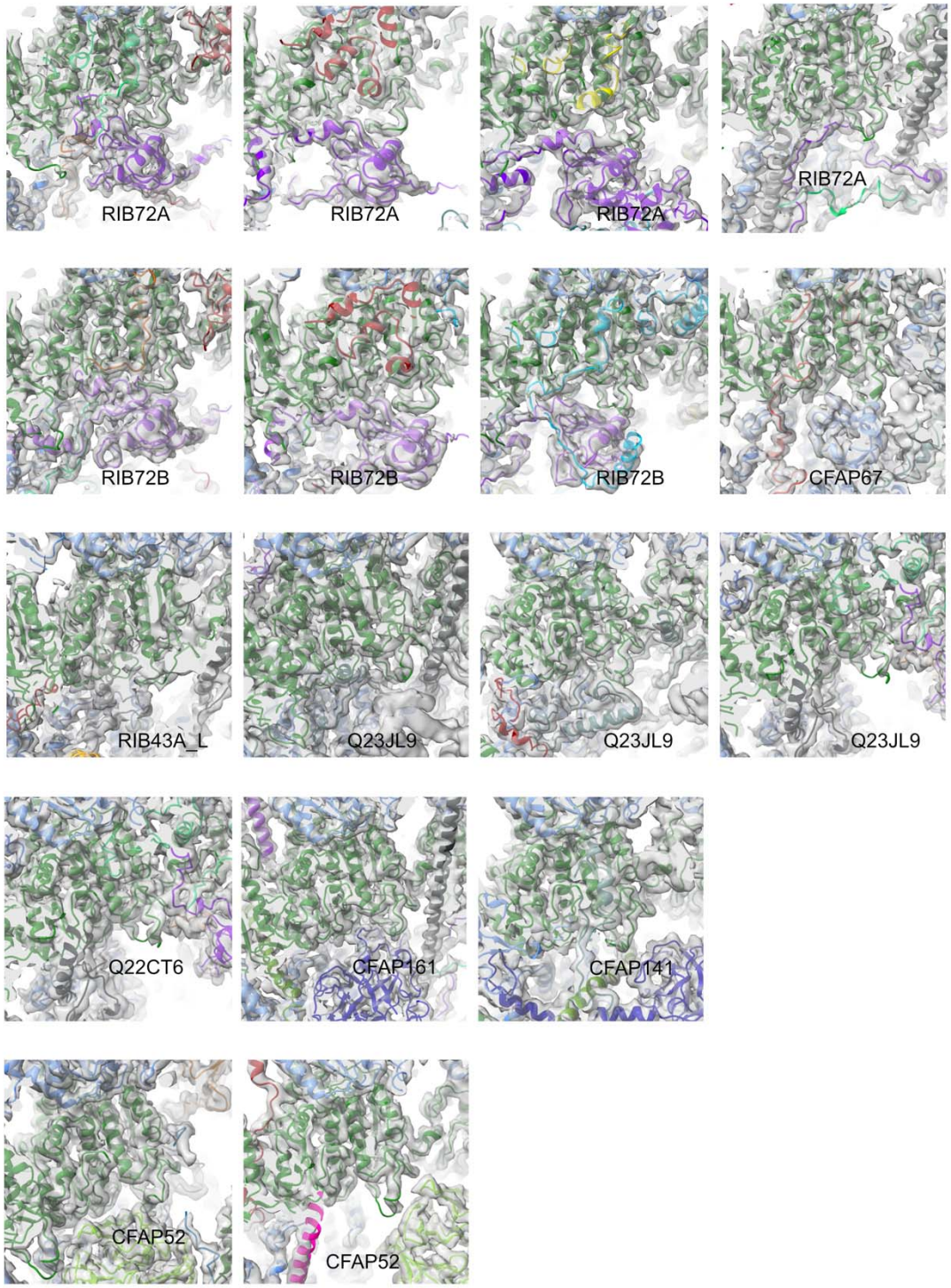

Figure S2. Diverse structures of the αK40 loops. Cryo-EM maps and models of partial and full αK40 loops in A2 (A-C), A10 (D-F), B1 (G-I), from *WT, K40R,* and *MEC17-KO Tetrahymena* strains.

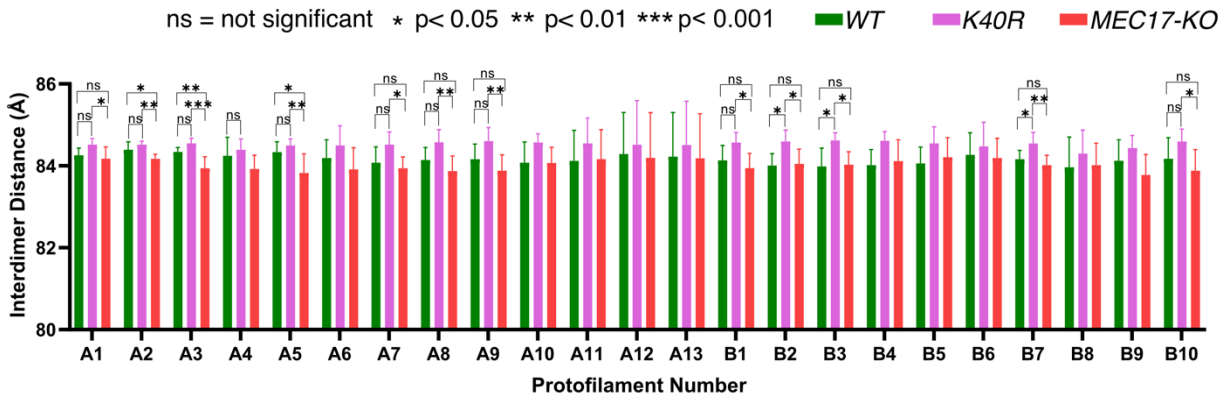

Figure S3. Interdimer distance within the same PF measured from cryo-EM density maps of *WT, K40R*, and *MEC17-KO Tetrahymena* species.

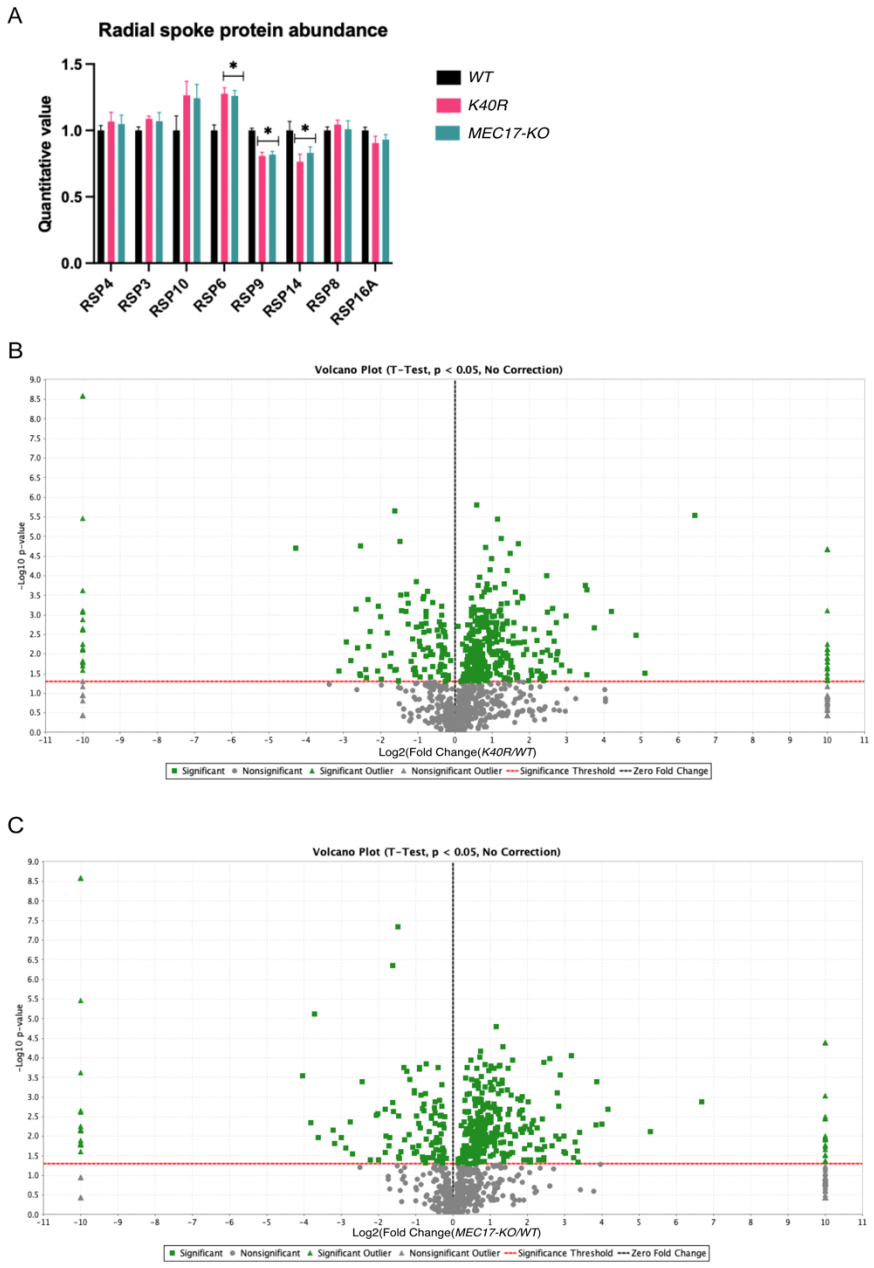

Figure S4. Mass spectrometry analysis of *WT*, *K40R* and *MEC17-KO*

(A) Radial spoke protein abundance in mass spectrometry triplicates of *WT*, *K40R*, and *MEC17-KO Tetrahymena* species. Asterisk (*) indicates a significant difference with $p < 0.05$. (B) Volcano plot showing up- and downregulated proteins in *K40R* mutants compared against *WT*, y-axis showing the -Log10 p values, and x-axis showing the Log2-fold change where negative and positive values suggest potential downregulation and upregulation, respectively. (C) Volcano plot showing up- and downregulated proteins in *MEC17-KO* mutants compared to *WT*.

Table S1. Count of full, partial, and missing αK40 loops based upon the *K40R* cryo-EM density maps, along with possible MIP interactions for αK40 loops in each PF.

Protofilament (48-nm Internal Repeat)	Full αK40 Loop Count	Partial αK40 Loop Count	Possible MIP Interaction
A1	6	0	RIB72A, RIB72B
A2	0	0	RIB72A, RIB72B, CFAP115
A3	6	0	RIB72A, RIB72B
A4	0	3	RIB72A, RIB72B
A5	6	0	RIB72A, RIB72B
A6	1	1	STPG2
A7	1	0	CFAP127
A8	0	0	
A9	3	0	CFAP67, CFAP161A, CFAP129, RIB57
A10	4	1	CFAP141, CFAP143, CFAP161A, RIB38
A11	3	2	CFAP143, CFAP161, RIB38, RIB57
A12	5	1	RIB43A_L, RIB72A
A13	1	3	RIB72B, RIB27B
B1	3	0	CFAP77, OJ2
B2	0	0	
B3	0	0	
B4	0	0	
B5	0	0	
B6	0	0	
B7	0	0	
B8	0	0	
B9	3	0	CFAP52, CFAP210, CFAP45
B10	3	0	CFAP52, PACRGA

Table S2. Inter-PF angles between subsequent PF obtained from cryo-EM maps of *WT*, *K40R*, and *MEC17-KO Tetrahymena* cilia.

	WT		*K40R*		*MEC17-KO*	
PF pair	**Mean rotation angle (degrees) n = 6**	**Standard Deviation**	**Mean rotation angle (degrees) n = 6**	**Standard Deviation**	**Mean rotation angle (degrees) n = 6**	**Standard Deviation**
A1_A2	26.454	0.230	25.987	0.415	26.356	0.281
A2_A3	34.578	0.318	34.270	0.338	34.391	0.364
A3_A4	28.017	0.238	28.247	0.262	28.279	0.475
A4_A5	27.823	0.522	27.716	0.422	28.152	0.615
A5_A6	22.892	0.633	23.306	0.416	22.996	0.546
A6_A7	21.501	0.671	21.392	0.349	21.138	0.362
A7_A8	32.418	0.570	32.577	0.577	32.339	0.528
A8_A9	22.918	0.535	22.930	0.413	22.971	0.399
A9_A10	41.819	0.604	41.593	0.656	42.305	0.431
A10_A11	29.368	0.610	28.645	0.626	28.851	0.438
A11_A12	20.461	0.520	20.878	0.573	20.311	0.557
A12_A13	15.875	0.491	16.399	0.581	16.007	0.626
A13_A1	35.974	0.370	36.050	0.481	36.173	0.464
B1_B2	22.161	0.240	21.737	0.158	22.059	0.141
B2_B3	22.579	0.272	22.384	0.252	22.385	0.217
B3_B4	22.919	0.193	23.447	0.283	23.258	0.439
B4_B5	23.137	0.448	23.839	0.397	23.232	0.407
B5_B6	23.211	0.639	24.329	0.245	23.359	0.261
B6_B7	20.003	0.468	20.688	0.361	19.951	0.418
B7_B8	29.039	0.351	23.353	0.624	27.737	0.481
B8_B9	21.829	0.385	22.303	0.466	21.939	0.554
B9_B10	23.554	0.455	27.409	0.417	24.556	0.527

Table S3. ANOVA test p values and significance of the interdimer distances of tubulin subunits within each PF in *WT, K40R*, and *MEC17-KO Tetrahymena* cilia.

PF	Interdimer distances from *WT* (Å) (mean ± SD, n = 6)	Interdimer distances from *K40R* (Å) (mean ± SD, n = 6)	Interdimer distances from *MEC17-KO* (Å) (mean ± SD, n = 6)	ANOVA p values	p value summary
A1	84.352 ± 0.276	84.518 ± 0.137	84.194 ± 0.221	0.097	ns
A2	84.453 ± 0.144	84.512 ± 0.083	84.222 ± 0.085	0.002	**
A3	84.426 ± 0.301	84.548 ± 0.113	84.218 ± 0.090	0.048	*
A4	84.300 ± 0.451	84.390 ± 0.244	84.016 ± 0.210	0.190	ns
A5	84.506 ± 0.268	84.493 ± 0.151	84.080 ± 0.195	0.009	**
A6	84.479 ± 0.473	84.495 ± 0.441	84.105 ± 0.388	0.305	ns
A7	84.418 ± 0.537	84.519 ± 0.282	84.091 ± 0.246	0.207	ns
A8	84.367 ± 0.298	84.575 ± 0.280	84.093 ± 0.191	0.034	*
A9	84.393 ± 0.428	84.603 ± 0.301	84.132 ± 0.351	0.157	ns
A10	84.364 ± 0.331	84.567 ± 0.195	84.141 ± 0.286	0.082	ns
A11	84.352 ± 0.639	84.546 ± 0.565	84.166 ± 0.636	0.629	ns
A12	84.323 ± 1.063	84.511 ± 0.989	84.198 ± 1.000	0.888	ns
A13	84.355 ± 0.957	84.506 ± 0.977	84.204 ± 1.018	0.890	ns
B1	84.253 ± 0.301	84.566 ± 0.226	84.136 ± 0.296	0.068	ns
B2	84.171 ± 0.302	84.592 ± 0.257	84.106 ± 0.343	0.046	*
B3	84.174 ± 0.413	84.617 ± 0.175	84.112 ± 0.255	0.034	*
B4	84.134 ± 0.359	84.607 ± 0.211	84.185 ± 0.417	0.085	ns
B5	84.036 ± 0.515	84.547 ± 0.368	84.133 ± 0.512	0.223	ns
B6	84.419 ± 0.358	84.473 ± 0.538	84.090 ± 0.617	0.465	ns
B7	84.042 ± 0.356	84.540 ± 0.252	84.271 ± 0.177	0.035	*
B8	84.129 ± 0.494	84.299 ± 0.525	84.061 ± 0.516	0.754	ns
B9	84.259 ± 0.371	84.432 ± 0.285	84.062 ± 0.446	0.321	ns
B10	84.359 ± 0.575	84.590 ± 0.281	84.194 ± 0.507	0.431	ns

Table S4. Proteins downregulated at least twofold in the *K40R* mutant compared to the *WT*.

Gene name	Gene ID	UniProt ID	Average *WT*	Average K40R	p value	Average fold change	Homolog in *C. reinhardtii*	Homolog in *Homo sapiens*
Dynein light chain 4	TTHERM_00716250	I7MCM8	12.080	3.057	0.001	0.300	NA	NA
Cell surface immobilization antigen SerH6, putative	TTHERM_00491130	Q23J59	14.630	3.516	0.001	0.200	A0A250XQN9	NA
CAMP-dependent kinase, regulatory protein	TTHERM_00623090	Q240X5	31.120	6.484	0.003	0.200	NA	NA
Tetratricopeptide repeat protein	TTHERM_00313720	Q22KA9	7.900	1.592	0.006	0.200	IFT70	Q8N4P2
CGMP-dependent kinase 5-1	TTHERM_00046530	Q23DN8	1.860	0.357	0.025	0.200	NA	NA
Glutathione S-transferase, amine-terminal domain protein	TTHERM_00602870	Q22YK8	6.730	1.172	0.000	0.200	NA	P09488
Heat shock 70 kDa protein	TTHERM_00105110	Q234I5	5.110	2.042	0.001	0.200	NA	NA
Uncharacterized protein	TTHERM_00455660	I7MI64	2.320	0.403	0.035	0.200	NA	NA

Table S5. Proteins upregulated at least twofold in the *K40R* mutant compared to *WT*

Gene name	Gene ID	UniProt ID	Avg *WT*	Avg *K40R*	p value	Average fold change	Homolog in *C. reinhardtii*	Homolog in *Homo sapiens*
WD domain, G-beta repeat protein	TTHERM_00006270	Q22SA9	1.160	4.649	0.047	4.000	NA	NA
Uncharacterized protein	TTHERM_00449680	Q238V2	0.460	1.932	0.026	4.200	NA	NA
Uncharacterized protein	TTHERM_00703420	Q22GI1	3.250	13.702	0.035	4.200	NA	NA
Uncharacterized protein	TTHERM_00392650	Q233I4	1.860	8.598	0.010	4.400	NA	NA
Uncharacterized protein	TTHERM_00548020	I7MDA2	1.860	8.598	0.005	4.600	NA	NA
SelT/selW/selH selenoprotein domain protein	TTHERM_00195980	Q23K36	0.460	2.289	0.042	4.900	NA	NA
FAM184 domain-containing protein	TTHERM_01321540	Q232U4	0.930	4.649	0.033	5.000	NA	Q8NB25
Calmodulin	NA	P02598	0.930	4.734	0.038	5.100	NA	Calmodulin 1,2,3
Dynein light chain 8-like E	NA	Q1HFV9	0.930	5.006	0.036	5.400	NA	P63167
Uncharacterized protein	TTHERM_00847020	Q22US8	0.700	3.927	0.008	5.600	NA	NA
Kinesin-like protein	TTHERM_01347910	Q229Q4	0.470	2.700	0.003	5.800	NA	Q2TAC6
Uncharacterized protein	TTHERM_00483660	I7M1N4	0.460	2.700	0.003	5.800	NA	NA
Cyclic nucleotide-binding domain protein	TTHERM_00841230	I7M4G5	0.460	2.700	0.003	5.800	NA	NA
Kinesin-like protein	TTHERM_00758880	Q23JL7	0.460	2.747	0.011	5.900	A0A2K3D1C7	A0A7I2V3N5
Scp-like extracellular protein,	TTHERM_00145900	I7MI85	1.620	10.088	0.001	6.200	NA	NA
Uncharacterized protein	TTHERM_00659030	I7M3P7	1.160	7.762	0.014	6.700	NA	NA
Hect domain and RCC1-like domain protein	TTHERM_00535910	I7LX15	0.700	4.696	0.010	6.800	NA	NA
Uncharacterized protein	TTHERM_00827160	Q22EF3	0.460	3.159	0.009	6.800	A0A2K3DZJ7	NA
Uncharacterized protein	TTHERM_000732839	W7XGQ6	0.930	7.341	0.001	7.900	NA	NA
Uncharacterized protein	TTHERM_00939090	Q22DN4	0.230	1.987	0.027	8.500	NA	NA
Uncharacterized protein	TTHERM_00388510	Q23RD8	1.160	13.239	0.000	11.000	NA	NA
B-box zinc finger protein	TTHERM_00112790	Q22Z92	0.230	2.692	0.033	12.000	NA	NA
Cyclic nucleotide-binding domain protein	TTHERM_00143540	I7M0S4	0.230	3.104	0.002	13.000	NA	NA
Uncharacterized protein	TTHERM_00497130	I7M4M1	0.230	4.284	0.000	18.000	NA	NA
EF hand protein	TTHERM_00833830	Q23A35	0.230	8.017	0.031	34.000	NA	NA

Table S6. Proteins downregulated at least twofold in the *MEC17-KO* mutant compared to the *WT*

Gene name	**Gene ID**	**UniProt ID**	**Avg WT**	**Avg *MEC17-KO***	**p value**	**Average fold change**	**Homolog in *C. reinhardtii***	**Homolog in *Homo sapiens***
CAMP-dependent kinase catalytic subunit	TTHERM_00433420	Q231B5	14.860	3.669	0.000	0.200	NA	NA
CAMP-dependent kinase, regulatory protein	TTHERM_00623090	Q240X5	31.120	7.513	0.003	0.200	NA	NA
Tetratricopeptide repeat	TTHERM_00313720	Q22KA9	7.900	1.471	0.000	0.200	A8ITN7	Q8N4P2
Uncharacterized protein	TTHERM_00455660	I7MI64	2.320	0.359	0.029	0.200	NA	NA
Metallo-beta-lactamase family protein	TTHERM_00128670	I7M1D2	9.530	1.418	0.004	0.100	NA	NA
Intraflagellar transporter-like protein	TTHERM_00648910	I7LT74	3.250	0.359	0.015	0.100	IFT54	IFT54
Uncharacterized protein	TTHERM_01106190	Q22BD8	4.410	0.359	0.011	0.080	NA	NA
Intraflagellar transporter-like protein, putative	TTHERM_00149230	I7LWB4	5.800	0.412	0.005	0.070	IFT74	IFT74

Table S7. Proteins upregulated least twofold in the *MEC17-KO* mutant compared to the *WT*

Gene name	Gene ID	UniProt ID	Avg *WT*	Avg K40R	p value	Average fold change	Homolog in *C. reinhardtii*	Homolog in *Homo sapiens*
Uncharacterized protein	TTHERM_00852750	Q24E65	4.180	16.987	0.001	4.100	NA	NA
Uncharacterized protein	TTHERM_00483660	I7M1N4	0.460	1.883	0.041	4.100	NA	NA
Uncharacterized protein	TTHERM_00219140	I7M2G4	1.620	6.778	0.007	4.200	NA	NA
Hect domain and RCC1-like domain protein	TTHERM_00535910	I7LX15	0.700	2.942	0.041	4.200	NA	NA
Uncharacterized protein	TTHERM_00703420	Q22GI1	3.250	13.940	0.008	4.300	NA	NA
Uncharacterized protein	TTHERM_00190760	I7M812	1.630	7.137	0.005	4.400	NA	NA
Dynein light chain 8-like E	NA	Q1HFV9	0.930	4.474	0.006	4.800	NA	P63167
Uncharacterized protein	TTHERM_00085240	Q236S4	0.230	1.121	0.021	4.800	NA	NA
Uncharacterized protein	TTHERM_00670810	I7LXT5	0.470	2.242	0.021	4.800	NA	NA
Uncharacterized protein	TTHERM_00468010	I7MAL9	0.930	4.536	0.022	4.900	NA	NA
Uncharacterized protein	TTHERM_00010960	Q22S36	0.690	3.415	0.040	4.900	NA	NA
Uncharacterized protein	TTHERM_00548020	I7MDA2	1.860	10.088	0.000	5.400	NA	NA
Kinesin-like protein	TTHERM_00794640	Q23VW7	0.470	2.592	0.018	5.500	NA	A0A7I2V3V3
Uncharacterized protein	TTHERM_00334380	I7M866	0.460	2.539	0.040	5.500	NA	NA
Cyclic nucleotide-binding domain protein	TTHERM_00841230	I7M4G5	0.460	2.539	0.040	5.500	NA	NA
Uncharacterized protein	TTHERM_00392650	Q233I4	0.700	4.772	0.010	6.800	NA	NA
Uncharacterized protein	TTHERM_00388510	Q23RD8	1.160	8.555	0.000	7.400	NA	NA
Uncharacterized protein	TTHERM_00827160	Q22EF3	0.460	3.354	0.012	7.200	NA	NA
Uncharacterized protein	TTHERM_000732839	W7XGQ6	0.930	7.329	0.010	7.900	NA	NA
Uncharacterized protein	TTHERM_00732900	Q245C1	0.460	3.669	0.024	7.900	NA	NA
Uncharacterized protein	TTHERM_001092361	W7X1T3	0.230	1.892	0.028	8.100	A0A2K3DJC4	NA
Uncharacterized protein	TTHERM_00825250	I7MCE2	0.230	1.892	0.028	8.100	NA	NA
Uncharacterized protein	TTHERM_00194430	Q23K92	0.930	8.555	0.000	9.200	NA	NA
Uncharacterized protein	TTHERM_01028860	Q23EF4	0.230	2.189	0.035	9.500	NA	NA
Uncharacterized protein	TTHERM_00078910	Q23FX3	0.470	4.536	0.014	9.700	NA	NA
Uncharacterized protein	TTHERM_00449080	Q239A7	0.470	4.728	0.024	10.000	NA	NA
Uncharacterized protein	TTHERM_01009900	Q23LQ6	0.230	3.363	0.000	15.000	NA	NA
Protein kinase	TTHERM_00497440	I7MB56	0.230	3.774	0.005	16.000	NA	NA
Cyclic nucleotide-binding domain protein	TTHERM_00143540	I7M0S4	0.230	4.124	0.002	18.000	NA	NA

References

Abraham, M. J., Murtola, T., Schulz, R., Páll, S., Smith, J. C., Hess, B., & Lindahl, E. (2015). GROMACS: High performance molecular simulations through multi-level parallelism from laptops to supercomputers. *SoftwareX, 1-2*, 19-25. doi:https://doi.org/10.1016/j.softx.2015.06.001

Akella, J. S., Wloga, D., Kim J., Starostina, N. G., Lyons-Abbott, S., Morrissette, N. S., . . . Gaertig, J. (2010). MEC-17 is an alpha-tubulin acetyltransferase. *Nature*(1476-4687 (Electronic)). doi:https://doi.org/10.1038/nature09324

Bustamante-Marin, X. M., & Ostrowski, L. E. (2017). Cilia and Mucociliary Clearance. *Cold Spring Harbor perspectives in biology, 9*(4), a028241. doi:10.1101/cshperspect.a028241

Cueva, J. G., Hsin, J., Huang, K. C., & Goodman, M. B. (2012). Posttranslational acetylation of alpha-tubulin constrains protofilament number in native microtubules. *Curr Biol, 22*(12), 1066-1074. doi:10.1016/j.cub.2012.05.012

Cueva, J. G., J., H., & Huang, K. C. G., Miriam B. (2012). Posttranslational acetylation of α-tubulin constrains protofilament number in native microtubules. *Curr Biol, 22*(12), 1066-1074. doi:10.1016/j.cub.2012.05.012

Djenoune, L., & Wyart, C. (2017). Light on a sensory interface linking the cerebrospinal fluid to motor circuits in vertebrates. *J Neurogenet, 31*(3), 113-127. doi:10.1080/01677063.2017.1359833

Du, Y., Seibenhener, M. L., Yan, J., Jiang, J., & Wooten, M. C. (2015). aPKC phosphorylation of HDAC6 results in increased deacetylation activity. *PLoS One, 10*(4), e0123191. doi:10.1371/journal.pone.0123191

Elam, C. A., Wirschell, M., Yamamoto, R., Fox, L. A., York, K., Kamiya, R., . . . Sale, W. S. (2011). An axonemal PP2A B-subunit is required for PP2A localization and flagellar motility. *Cytoskeleton (Hoboken), 68*(7), 363-372. doi:10.1002/cm.20519

Eshun-Wilson, L., Zhang, R., Portran, D., Nachury, M. V., Toso, D. B., Löhr, T., . . . Nogales, E. (2019). Effects of α-tubulin acetylation on microtubule structure and stability. *Proceedings of the National Academy of Sciences, 116*(21), 10366. doi:10.1073/pnas.1900441116

Fukushige, T., Hendzel, M. J., Bazett-Jones, D. P., & McGhee, J. D. (1999). Direct visualization of the elt-2 gut-specific GATA factor binding to a target promoter inside the living Caenorhabditis elegans embryo. *Proc Natl Acad Sci U S A, 96*(21), 11883-11888. doi:10.1073/pnas.96.21.11883

Gadadhar, S., Viar, G. A., Hansen, J. N., Gong, A., Kostarev, A., Ialy-Radio, C., . . . Janke, C. (2021). Tubulin glycylation controls axonemal dynein activity, flagellar beat, and male fertility. *Science, 371*(6525), eabd4914. doi:doi:10.1126/science.abd4914

Gaertig, J., Cruz, M. A., Bowen, J., Gu, L., Pennock, D. G., & Gorovsky, M. A. (1995). Acetylation of lysine 40 in alpha-tubulin is not essential in Tetrahymena thermophila. *J Cell Biol, 129*(5), 1301-1310. doi:10.1083/jcb.129.5.1301

Garnham, C. P., & Roll-Mecak, A. (2012). The chemical complexity of cellular microtubules: tubulin post-translational modification enzymes and their roles in tuning microtubule functions. *Cytoskeleton (Hoboken), 69*(7), 442-463. doi:10.1002/cm.21027

Gorovsky, M. A., Yao, M. C., Keevert, J. B., & Pleger, G. L. (1975). Isolation of micro- and macronuclei of Tetrahymena pyriformis. *Methods Cell Biol, 9*(0), 311-327. doi:10.1016/s0091-679x(08)60080-1

Howes, S. C., Alushin, G. M., Shida, T., Nachury, M. V., & Nogales, E. (2014). Effects of tubulin acetylation and tubulin acetyltransferase binding on microtubule structure. *Mol Biol Cell, 25*(2), 257-266. doi:10.1091/mbc.E13-07-0387

Hubbert, C., A, G., Shao, R., Kawaguchi, Y., Ito, A., Nixon, A., . . . Yao, T. P. (2002). HDAC6 is a microtubule-associated deacetylase. *Nature*(0028-0836 (Print)).

Ichikawa, M., Khalifa, A. A. Z., Kubo, S., Dai, D., Basu, K., Maghrebi, M. A. F., . . . Bui, K. H. (2019). Tubulin lattice in cilia is in a stressed form regulated by microtubule inner proteins. *Proceedings of the National Academy of Sciences, 116*(40), 19930-19938. doi:10.1073/pnas.1911119116

Ichikawa, M., Liu, D., Kastritis, P. L., Basu, K., Hsu, T. C., Yang, S., & Bui, K. H. (2017). Subnanometre-resolution structure of the doublet microtubule reveals new classes of microtubule-associated proteins. *Nature Communications, 8*(1), 15035. doi:10.1038/ncomms15035

Johnson, K. A. (1998). The axonemal microtubules of the Chlamydomonas flagellum differ in tubulin isoform content. *J Cell Sci, 111 (Pt 3)*(0021-9533 (Print)), 313-320. doi:10.1242/jcs.111.3.313

Jorgensen, W. L., & Tirado-Rives, J. (2005). Potential energy functions for atomic-level simulations of water and organic and biomolecular systems. *Proceedings of the National Academy of Sciences, 102*(19), 6665-6670. doi:10.1073/pnas.0408037102

Kalebic, N., S., S., E, P., G, B., C, M., & Heppenstall, P. A. (2013). αTAT1 is the major α-tubulin acetyltransferase in mice. *Nat Commun*(2041-1723 (Electronic)).

Kaul, N., Soppina, V., & Verhey, K. J. (2014). Effects of alpha-tubulin K40 acetylation and detyrosination on kinesin-1 motility in a purified system. *Biophys J, 106*(12), 2636-2643. doi:10.1016/j.bpj.2014.05.008

Kenzaki, H., Koga, N., Hori, N., Kanada, R., Li, W., Okazaki, K.-i., . . . Takada, S. (2011). CafeMol: A Coarse-Grained Biomolecular Simulator for Simulating Proteins at Work. *Journal of Chemical Theory and Computation, 7*(6), 1979-1989. doi:10.1021/ct2001045

Khalifa, A., Ichikawa, M., Dai, D., Kubo, S., Black, C., Peri, K., . . . Bui, K. (2020). The inner junction complex of the cilia is an interaction hub that involves tubulin post-translational modifications. *Elife*(2050-084X (Electronic)).

Kubo, S., Black, C. S., Joachimiak, E., Yang, S. K., Legal, T., Peri, K., . . . Bui, K. H. (2023). Native doublet microtubules from Tetrahymena thermophila reveal the importance of outer junction proteins. *Nature Communications, 14*(1), 2168. doi:10.1038/s41467-023-37868-0

Kubo, T., Hirono, M., Aikawa, T., Kamiya, R., & Witman, G. B. (2015). Reduced tubulin polyglutamylation suppresses flagellar shortness in Chlamydomonas. *Mol Biol Cell, 26*(15), 2810-2822. doi:10.1091/mbc.E15-03-0182

Kubo, T., Yanagisawa, H.-a., Yagi, T., Hirono, M., & Kamiya, R. (2010). Tubulin Polyglutamylation Regulates Axonemal Motility by Modulating Activities of Inner-Arm Dyneins. *Current Biology, 20*(5), 441-445. doi:https://doi.org/10.1016/j.cub.2009.12.058

Lechtreck, K. F., & Geimer, S. (2000). Distribution of polyglutamylated tubulin in the flagellar apparatus of green flagellates. *Cell Motil Cytoskeleton, 47*(3), 219-235. doi:10.1002/1097-0169(200011)47:3<219::AID-CM5>3.0.CO;2-Q

Legal, T., Tong, M., Black, C., Paterno, M. V., Gaertig, J., & Bui, K. H. (2023). Molecular architecture of the ciliary tip revealed by cryo-electron tomography. *bioRxiv*, 2023.2001.2003.522627. doi:10.1101/2023.01.03.522627

Lehti, M. S., & Sironen, A. (2017). Formation and function of sperm tail structures in association with sperm motility defects†. *Biology of Reproduction, 97*(4), 522-536. doi:10.1093/biolre/iox096

Li, W., Terakawa, T., Wang, W., & Takada, S. (2012). Energy landscape and multiroute folding of topologically complex proteins adenylate kinase and 2ouf-knot. *Proceedings of the National Academy of Sciences, 109*(44), 17789-17794. doi:10.1073/pnas.1201807109

Li, W., Wang, W., & Takada, S. (2014). Energy landscape views for interplays among folding, binding, and allostery of calmodulin domains. *Proceedings of the National Academy of Sciences, 111*(29), 10550-10555. doi:10.1073/pnas.1402768111

Liu, N., Xiong, Y., Li, S., Ren, Y., He, Q., Gao, S., . . . Shui, W. (2015). New HDAC6-mediated deacetylation sites of tubulin in the mouse brain identified by quantitative mass spectrometry. *Scientific Reports, 5*(1), 16869. doi:10.1038/srep16869

M, L., & Piperno, G. (1987). Identification of an acetylation site of Chlamydomonas alpha-tubulin. *Proc Natl Acad Sci U S A*
. (0027-8424 (Print)).

Ma, M., Stoyanova, M., Rademacher, G., Dutcher, S. K., Brown, A., & Zhang, R. (2019). Structure of the Decorated Ciliary Doublet Microtubule. *Cell, 179*(4), 909-922.e912. doi:https://doi.org/10.1016/j.cell.2019.09.030

Margreitter, C., Petrov, D., & Zagrovic, B. (2013). Vienna-PTM web server: a toolkit for MD simulations of protein post-translational modifications. *Nucleic Acids Research, 41*(W1), W422-W426. doi:10.1093/nar/gkt416

Margreitter, C., Reif, M. M., & Oostenbrink, C. (2017). Update on phosphate and charged post-translationally modified amino acid parameters in the GROMOS force field. *Journal of Computational Chemistry, 38*(10), 714-720. doi:https://doi.org/10.1002/jcc.24733

North, B. J., Bl, M., Mt, B., Jm, D., & Verdin, E. (2003). The human Sir2 ortholog, SIRT2, is an NAD+-dependent tubulin deacetylase. *Mol Cell*
.(1097-2765 (Print)).

Pathak, N., Austin-Tse, C. A., Liu, Y., Vasilyev, A., & Drummond, I. A. (2014). Cytoplasmic carboxypeptidase 5 regulates tubulin glutamylation and zebrafish cilia formation and function. *Mol Biol Cell, 25*(12), 1836-1844. doi:10.1091/mbc.E13-01-0033

Pathak, N., Obara, T., Mangos, S., Liu, Y., & Drummond, I. A. (2007). The zebrafish fleer gene encodes an essential regulator of cilia tubulin polyglutamylation. *Mol Biol Cell, 18*(11), 4353-4364. doi:10.1091/mbc.e07-06-0537

Petrov, D., Margreitter, C., Grandits, M., Oostenbrink, C., & Zagrovic, B. (2013). A Systematic Framework for Molecular Dynamics Simulations of Protein Post-Translational Modifications. *PLOS Computational Biology, 9*(7), e1003154. doi:10.1371/journal.pcbi.1003154

Pettersen, E. F., Goddard, T. D., Huang, C. C., Couch, G. S., Greenblatt, D. M., Meng, E. C., & Ferrin, T. E. (2004). UCSF Chimera—A visualization system for exploratory research and analysis. *Journal of Computational Chemistry, 25*(13), 1605-1612. doi:https://doi.org/10.1002/jcc.20084

Porter, M. E., & Sale, W. S. (2000). The 9 + 2 axoneme anchors multiple inner arm dyneins and a network of kinases and phosphatases that control motility. *J Cell Biol, 151*(5), F37-42. doi:10.1083/jcb.151.5.f37

Pronk, S., Páll, S., Schulz, R., Larsson, P., Bjelkmar, P., Apostolov, R., . . . Lindahl, E. (2013). GROMACS 4.5: a high-throughput and highly parallel open source molecular simulation toolkit. *Bioinformatics, 29*(7), 845-854. doi:10.1093/bioinformatics/btt055

Ran, J., Yang, Y., Li, D., Liu, M., & Zhou, J. (2015). Deacetylation of α-tubulin and cortactin is required for HDAC6 to trigger ciliary disassembly. *Sci Rep*
. (2045-2322 (Electronic)).

Reed, N. A., Cai, D., Blasius, T. L., Jih, G. T., Meyhofer, E., Gaertig, J., & Verhey, K. J. (2006). Microtubule Acetylation Promotes Kinesin-1 Binding and Transport. *Current Biology, 16*(21), 2166-2172. doi:https://doi.org/10.1016/j.cub.2006.09.014

Rogowski, K., Francois, J., van Dijk, J., Wloga, D., Strub, J.-M., Levilliers, N., . . . Janke, C. (2019). Evolutionary divergence of enzymatic mechanisms for posttranslational polyglycylation. *Cell, 137*(6), 1076-1087.

Rogowski, K., van Dijk, J., Magiera, M. M., Bosc, C., Deloulme, J.-C., Bosson, A., . . . Janke, C. (2010a). A family of protein-deglutamylating enzymes associated with neurodegeneration. *Cell, 143*(4), 564-578. doi:10.1016/j.cell.2010.10.014

Rogowski, K., van Dijk, J., Magiera, M. M., Bosc, C., Deloulme, J. C., Bosson, A., . . . Janke, C. (2010b). A family of protein-deglutamylating enzymes associated with neurodegeneration. *Cell, 143*(4), 564-578. doi:10.1016/j.cell.2010.10.014

Šali, A., & Blundell, T. L. (1993). Comparative Protein Modelling by Satisfaction of Spatial Restraints. *Journal of Molecular Biology, 234*(3), 779-815. doi:https://doi.org/10.1006/jmbi.1993.1626

Sanchez-Garcia, R., Gomez-Blanco, J., Cuervo, A., Carazo, J. M., Sorzano, C. O. S., & Vargas, J. (2021). DeepEMhancer: a deep learning solution for cryo-EM volume post-processing. *Communications Biology, 4*(1), 874. doi:10.1038/s42003-021-02399-1

Saunders, H. A. J., Johnson-Schlitz, D. M., Jenkins, B. V., Volkert, P. J., Yang, S. Z., & Wildonger, J. (2022). Acetylated α-tubulin K394 regulates microtubule stability to shape the growth of axon terminals. *Current Biology, 32*(3), 614-630.e615. doi:10.1016/j.cub.2021.12.012

Schaedel, L., John, K., Gaillard, J., Nachury, M. V., Blanchoin, L., & Thery, M. (2015). Microtubules self-repair in response to mechanical stress. *Nat Mater, 14*(11), 1156-1163. doi:10.1038/nmat4396

Schmid, N., Eichenberger, A. P., Choutko, A., Riniker, S., Winger, M., Mark, A. E., & van Gunsteren, W. F. (2011). Definition and testing of the GROMOS force-field versions 54A7 and 54B7. *European Biophysics Journal, 40*(7), 843-856. doi:10.1007/s00249-011-0700-9

Shah, N., Kumar, S., Zaman, N., Pan, C. C., Bloodworth, J. C., Lei, W., . . . Lee, N. Y. (2018). TAK1 activation of alpha-TAT1 and microtubule hyperacetylation control AKT signaling and cell growth. *Nat Commun, 9*(1), 1696. doi:10.1038/s41467-018-04121-y

Shida, T., Cueva, J. G., Xu, Z., Goodman, M. B., & Nachury, M. V. (2010). The major alpha-tubulin K40 acetyltransferase alphaTAT1 promotes rapid ciliogenesis and efficient mechanosensation. *Proc Natl Acad Sci U S A, 107*(50), 21517-21522. doi:10.1073/pnas.1013728107

Sjostrand, F. S. (1953). The ultrastructure of the innersegments of the retinal rods of the guinea pig eye as revealed by electron microscopy. *J Cell Comp Physiol*(0095-9898 (Print)). doi:D - CLML: 5425:5457:294:405 OTO - NLM

Stoddard, D., Zhao, Y., Bayless, B. A., Gui, L., Louka, P., Dave, D., . . . Nicastro, D. (2018). Tetrahymena RIB72A and RIB72B are microtubule inner proteins in the ciliary doublet microtubules. *Molecular Biology of the Cell, 29*(21), 2566-2577. doi:10.1091/mbc.E18-06-0405

Suryavanshi, S., Eddé, B., Fox, L. A., Guerrero, S., Hard, R., Hennessey, T., . . . Gaertig, J. (2010). Tubulin Glutamylation Regulates Ciliary Motility by Altering Inner Dynein Arm Activity. *Current Biology, 20*(5), 435-440. doi:https://doi.org/10.1016/j.cub.2009.12.062

Sw, L. H., & Rosenbaum, J. L. (1983). Chlamydomonas alpha-tubulin is posttranslationally modified in the flagella during flagellar assembly. *J Cell Biol.* (0021-9525 (Print)).

Terakawa, T., & Takada, S. (2014). RESPAC: Method to Determine Partial Charges in Coarse-Grained Protein Model and Its Application to DNA-Binding Proteins. *Journal of Chemical Theory and Computation, 10*(2), 711-721. doi:10.1021/ct4007162

Viar, G. A., Klena, N., Martino, F., Nievergelt, A., & Pigino, G. (2023). The Tubulin Nano-Code: a protofilament-specific pattern of tubulin post-translational modifications regulates ciliary beating mechanics. *bioRxiv*, 2023.2006.2028.546853. doi:10.1101/2023.06.28.546853

Wang, W., & Brautigan, D. L. (2008). Phosphatase inhibitor 2 promotes acetylation of tubulin in the primary cilium of human retinal epithelial cells. *BMC Molecular and Cell Biology, 9*(62).

Williams, N. E., Wolfe, J., & Bleyman, L. K. (1980). Long-Term Maintenance of Tetrahymena Spp. *The Journal of Protozoology, 27*(3), 327-327. doi:https://doi.org/10.1111/j.1550-7408.1980.tb04270.x

Wloga, D., Dm, W., K, R., Mh, B., N, L., M, J.-D., . . . Gaertig, J. (2009). TTLL3 Is a tubulin glycine ligase that regulates the assembly of cilia. *Dev Cell*
. (1878-1551 (Electronic)).

Wloga, D., Joachimiak, E., Louka, P., & Gaertig, J. (2017). Posttranslational Modifications of Tubulin and Cilia. *Cold Spring Harb Perspect Biol, 9*(6). doi:10.1101/cshperspect.a028159

Wloga, D., K, R., N, S., J, V. D., C, J., B, E., . . . Gaertig, J. (2008). Glutamylation on alpha-tubulin is not essential but affects the assembly and functions of a subset of microtubules in Tetrahymena thermophila. *Eukaryot Cell*(1535-9786 (Electronic)).

Wloga, D., Webster, D. M., Rogowski, K., Bre, M. H., Levilliers, N., Jerka-Dziadosz, M., . . . Gaertig, J. (2009). TTLL3 Is a Tubulin Glycine Ligase that Regulates the Assembly of Cilia. *Developmental Cell, 16*(6), 867-876. doi:10.1016/j.devcel.2009.04.008

Xu, Z., Schaedel, L., Portran, D., Aguilar, A., Gaillard, J., Marinkovich, M. P., . . . Nachury, M. V. (2017). Microtubules acquire resistance from mechanical breakage through intralumenal acetylation. *Science, 356*(6335), 328-332. doi:10.1126/science.aai8764

Zhang, R., Alushin, G. M., Brown, A., & Nogales, E. (2015). Mechanistic Origin of Microtubule Dynamic Instability and Its Modulation by EB Proteins. *Cell, 162*(4), 849-859. doi:10.1016/j.cell.2015.07.012

Zhou, X., Fan, L. X., Li, K., Ramchandran, R., Calvet, J. P., & Li, X. (2014). SIRT2 regulates ciliogenesis and contributes to abnormal centrosome amplification caused by loss of polycystin-1. *Hum Mol Genet, 23*(6), 1644-1655. doi:10.1093/hmg/ddt556